

UC Irvine

UC Irvine Electronic Theses and Dissertations

Title

Metamaterial for Enhanced Sensing and Power Management Application

Permalink

<https://escholarship.org/uc/item/9vm988j9>

Author

YE, Fan

Publication Date

2024

Peer reviewed|Thesis/dissertation

UNIVERSITY OF CALIFORNIA,
IRVINE

Metamaterial for Enhanced Sensing and Power Management Application

DISSERTATION

submitted in partial satisfaction of the requirements
for the degree of

DOCTOR OF PHILOSOPHY

in Electrical and Computer Engineering

by

Fan Ye

Dissertation Committee:
Associate Professor Peter Tseng, Chair
Professor Fadi Kurdahi
Associate Professor Hung Cao

2024

DEDICATION

To my beloved parents, Qin and Ranchun,
whose love and support have been the foundation of my perseverance.

TABLE OF CONTENTS

	Page
LIST OF FIGURES	iv
ACKNOWLEDGMENTS	viii
VITA	ix
ABSTRACT OF THE DISSERTATION	xi
1 Introduction	1
2 Passive Sensor System Codesign Methodology	9
2.1 Tx+Sensor	9
2.2 Tx+Multi-Sensor	13
2.3 Tx+IR+Sensors	16
2.4 Tx+Resonate Coil Pair	18
3 Passive and Wireless, Ion-Selective Sensor Arrays for Multiminerall Comonitoring of Food	20
3.1 Sensing Methodology and Properties	20
3.2 Fabrication and Basic Response of Ion-Selective RF Sensors	23
3.3 Ion-Selective RF Sensor Arrays	25
4 Programmable Multiwavelength Radio Frequency Spectrometry of Chemophysical Environments through an Adaptable Network of Flexible and Environmentally Responsive, Passive Wireless Elements	32
5 Passive Wireless Body Joint-Monitoring Networks with Textile-Integrated, Strongly Coupled Magnetic Resonators	47
5.1 Operating Principle	47
5.2 Simulation and Calibration	50
5.3 Body Joint Monitoring Networks	55
Bibliography	58

LIST OF FIGURES

	Page
2.1 The equivalent circuit of the reader and RF sensor system. The mutual inductance(M) may take different values depending on the alignment between the reader and sensor.	10
2.2 Modifying the equivalent circuit of the reader and RF sensor system using the T model	10
2.3 The equivalent circuit of the larger reader and RF sensor system. The mutual inductance(M) may take different values depending on the alignment between the reader and sensor.	13
2.4 Modifying the equivalent circuit of the larger reader and RF sensor system using the T model	13
2.5 The equivalent circuit of the multi-port reader and RF sensor system. The mutual inductance(M) may take different values depending on the alignment between the reader and sensor.	15
2.6 Modifying the equivalent circuit of the multi-port reader and RF sensor system using the T model	15
2.7 The equivalent circuit of the reader, intermediate relay, and RF sensor system. The mutual inductance(M) may take different values depending on the alignment between the reader, intermediate relay, and sensor.	17
2.8 Modifying the equivalent circuit of the reader, intermediate relay, and RF sensor system using the T model	17
2.9 The equivalent circuit of the reader, sensor1 and sensor 2. The mutual inductance(M) may take different values depending on the alignment between the reader and sensors.	19
2.10 Plot $ S_{11} $ through eq 2.31 with components' value from Figure 1.9	19

3.1	Passive wireless ion-selective RF sensor arrays. a) RF ion-selective sensor fabrication process. b) RF sensors are arrayed to monitor multiple minerals. Herein we integrate calcium and magnesium ISM into respective sensors to facilitate measurement of these two key divalent ions. c) Simulated and measured spectral response of ion-selective RF sensors sized to different area footprints. Size measurement is in centimeters. d) Image of fabricated resonator. Scale bar is 8 cm. e) Simulation results of the sensor with i and without ii ions. The electric field is exclusively focused in between split rings to maximize sensor selectivity. With ion presence, the resonator absorbs more energy and exhibits larger electric field intensity. Scale bar is 1 mm	22
3.2	Ion-selective RF sensor performance parameters. a) Side-view schematic of calcium-selective RF sensor and membrane selectivity against sodium. b) Sensitivity and sodium selectivity of RF sensors ($N = 3$). c,d) Hysteresis and 10 d response of calcium-selective RF sensor. e) Side-view schematic of magnesium-selective RF sensor and membrane selectivity against sodium. f) Sensitivity and sodium selectivity of RF sensors ($N = 3$). g,h) Hysteresis and 10 d response of magnesium-selective RF sensor.	26
3.3	Ion-selective RF sensor characterization when in the presence of the divalent ion. a) Calcium ISM exhibits moderate selectivity against magnesium. b,c) Sensitivity and selectivity of calcium-selective RF sensor to calcium and magnesium in deionized water. $N = 3$. Curves can be fitted to individual sensor responses to describe its sensitivity to different ions. d) Magnesium ISM exhibits moderate selectivity against calcium. e,f) Sensitivity and selectivity of magnesium-selective RF sensor to magnesium and calcium in deionized water. $N = 3$. Like above, curves can be fitted to individual sensor responses to describe its sensitivity to different ions.	27
3.4	Optimized, food ware-integrated passive wireless network to measure divalent ions. a) Ion-selective RF sensors are oriented inside the cup. Outside the cup is a cup-conforming, custom readout coil that attaches and aligns adjacent to the sensor array. This readout coil exhibits nearfield magnetic hotspots that match sensor positioning. b) Circuit diagram of readout coil and sensor array. c,d) Respective RF sensor sensitivities calibrated in diluted milk. e) Reduced percent error measurement in a random grouping of magnesium/calcium concentrations enabled by our sensor measurement and basic numerical extraction approach.	31

4.1	Programmable multiwavelength RF spectrometry of the chemophysical environment. A) A network composed of multilayers of passive (zero-electronic) elements enables single readout monitoring of complex signals. (i) Circuit diagram of reader wirelessly coupled to an IR, in turn wirelessly coupled to tunable RF sensors, (ii) RF simulation of the spectral readout where sensor 1 is perturbed by both R1 and C1, sensor 2 is perturbed only in C2, and sensor 3 is perturbed only in R3, (iii) geometry used in finite element method (top) and corresponding magnetic field distribution showing magnetic coupling between elements. B) Flexible IR is integrated into the outer surface of cups. C) IR-integrated smart textile to facilitate multiparametric wristband readout. Insets are the placement of the wristband and direct readout from wearable NanoVNA. D) Readout antenna structures studied herein (i) circular without ground (CWOOG), (ii) circular with ground (CWG), and (iii) planar with ground (PWG). E) Spectral readout from various network configurations: single sensor without IR (diameter of the readout coil loop is 25 mm), multiple sensors without IR (diameter of the readout coil loop is 50 mm), and multiple sensors with IR (diameter of the IR loop is 50 mm). The standard vertical distance between the readout coil/IR loop and sensors is 0.5 mm. For multisensor readout, the orientation of the sensors remains constant. Scale bars are 5 cm.	34
4.2	Augmented readout via network coupling through an IR. A) Effect of the alignment between readout antenna and IR when IR and sensor orientation is fixed: (i) schematic presentation of the orientation of the antenna, IR, and sensor, network S11 response by (ii) CWOOG, and (iii) CWG. B) Effect of the alignment between IR and sensor while antenna and IR are fixed: (i) schematic of network orientation, network S11 response by (ii) CWOOG and (iii) CWG. C) Readout of multiple sensors through multiple IR. Network S11 response during (i) series and (ii) parallel extension. Insets are the network orientation. D) Readout of multiple sensors by IR. Effect of the alignment between readout antenna and IR when IR and sensor orientations are fixed: network S11 response by (i) CWOOG (ii) CWG. Inset is the network orientation.	37
4.3	Cross-coupling effect among sensors. A) Effect of positional coupling between sensors: (i) schematic presentation of sensor array orientation during experiment, and S11 response from sensors with (ii) CWOOG and (iii) CWG readout antennas. In between is a blow-up plot highlighting the shift or lack of shift in resonant frequency due to coupling. B) Effect of sensimetric coupling between sensors (applied pressure): (i) schematic presentation of applying stimuli to various sensors, and S11 response from sensors with (ii) CWOOG and (iii) CWG readout antennas. In between is a blow-up plot highlighting the shift in resonant frequency of the spectral peak linked to respective sensors. No other peak exhibits a shift.	41

4.4	Functional systems for monitoring chemophysical state. A) Multiparametric readout from a wearable wristband. B) Spectrometric readout of sensor state: (i) evolution of spectra after completed perturbations, and (ii-v) zoom-in of network S11 response due to modulating salt ($0-10\text{mgdL}^{-1}$), pH (4-7.4), temperature (40°C to room), and pressure (manual). C) A Smartcup for monitoring nutrients in a drink. D) Spectrometric readout of sensors state: (i) evolution of spectra after completed perturbations, and (ii-v) zoomed network S11 response of the sugar-optimized ($0-100\text{gdL}^{-1}$), salt-optimized ($0-25\text{mgdL}^{-1}$), fat-optimized ($0-20\mu\text{L}$), and temperature (50°C to room) sensors after completed perturbations. Scale bars are 2cm.	44
5.1	Design of strongly coupled resonators for joint angle monitoring. a) Diagram of sensing mechanism. b) Equivalent circuit of the strongly coupled resonators and resonance split with respect to coupling coefficient. c) Multiple joint monitoring diagram. d) Sensor fabrication and integration into textile. . . .	48
5.2	Simulation and validation of inductive joint monitoring scheme. a) Resonators can be shaped in simulation to mimic how they may be practically deformed on the curvature of the body. b) Magnetic field distribution at equivalent bending angles for different resonator deformation states. c) Simulated spectral response of resonator pair at different bending angles (30° to 110° every 10°). d) Comparison of the resonant frequency difference between simulation and experiment at different bending angles. $N = 3$ with error bars denoting standard deviation in measured frequency differential.	52
5.3	On-body joint angle measurement and calibration. The spectral response of our resonator scheme is plotted and compared against image-based body angle tracking. a) Resonators are attached to the elbow for rotation angle monitoring. b) Resonators are attached to elbow for bending/flexing angle monitoring. c) Resonators are attached to ankle for bending/flexing angle monitoring. d) Resonators are attached to the back knee for bending/flexing angle monitoring. The average for $N = 3$ and error bars represent the standard deviation for the right four plots.	54
5.4	Passive joint monitoring networks. a) Dynamic spectral response of resonator pair in benchtop settings. b) Real-time monitoring of knee and ankle joints during a variety of practical exercises. Each exercise exhibits unique signatures in measured joint angle response along the knee and ankle, respectively. Within the plots, the mean joint angle (as measured using user pictures) is labeled for respective exercises.	56

ACKNOWLEDGMENTS

I would like to express my deepest gratitude to my PhD supervisor, Prof. Peter Tseng, for his exceptional and unwavering support throughout my academic journey at UCI. I am truly thankful for his constant encouragement and for always standing by me. Prof. Tseng's guidance went beyond the technical aspects, encompassing logistics and resource management, and his understanding and support were crucial to the advancement of my research. He taught me to think beyond the ordinary and to continuously seek growth opportunities.

I am also grateful to my committee members, Prof. Fadi Kurdahi, Prof. Michelle Khine, and Prof. Hung Cao, for their invaluable support in fostering cross-functional collaborations.

This research was made possible through the faculty startup funds provided by the University of California, Irvine, and was further supported in part by the National Science Foundation (NSF) CAREER Award (Award number 1942364), as well as the CAREER award ECCS-1942364 received by Prof. Tseng.

VITA

Fan Ye

EDUCATION

Doctor of Philosophy in Computer Science
University of California, Irvine

2024
Irvine, CA

Bachelor of Science in Physics
Southern University of Science and Technology

2019
Shenzhen, Guangdong

RESEARCH EXPERIENCE

Graduate Research Assistant
University of California, Irvine

2020–2024
Irvine, California

JOURNAL PUBLICATIONS

1. Ye, Fan, Amirhossein Hajiaghajani, Amir Zargari, Alberto Escobar, Huiting Qin, Lei Li, Chengyang Qian et al. "Passive Wireless Body Joint-Monitoring Networks with Textile-Integrated, Strongly Coupled Magnetic Resonators." *Advanced Electronic Materials* (2024): 2400450.
2. Li, Lei, Fan Ye, Kazi Khurshidi Haque Dia, Alberto Ranier Escobar, Abeed Hasan, Huiting Qin, Jialin Lin, and Peter Tseng. "Passive and Wireless, Ion-Selective Sensor Arrays for Multimineral Comonitoring of Food." *Advanced Sensor Research* 3, no. 11 (2024): 2400054.
3. Dautta, Manik, Amirhossein Hajiaghajani, Fan Ye, Alberto Ranier Escobar, Abel Jimenez, Kazi Khurshidi Haque Dia, and Peter Tseng. "Programmable multiwavelength radio frequency spectrometry of chemophysical environments through an adaptable network of flexible and environmentally responsive, passive wireless elements." *Small Science* 2, no. 6 (2022): 2200013.
4. Qian, Chengyang, Fan Ye, Junye Li, Peter Tseng, and Michelle Khine. "Wireless and Battery-Free Sensor for Interstitial Fluid Pressure Monitoring." *Sensors* 24, no. 14 (2024): 4429.
5. Dia, Kazi Khurshidi Haque, Alberto Ranier Escobar, Huiting Qin, Fan Ye, Abel Jimenez, Md Abeed Hasan, Amirhossein Hajiaghajani, Manik Dautta, Lei Li, and Peter Tseng. "Passive Wireless Porous Biopolymer Sensors for At-Home Monitoring of Oil and Fatty Acid Nutrition." *ACS Applied Bio Materials* 7, no. 8 (2024): 5452-5460.
6. Li, Lei, Alberto R. Escobar, Somayeh Zanganeh, Manik Dautta, M. M. H. Sajeeb, Fan Ye, Jens T. Escobar, and Peter Tseng. "Mechanically-directed assembly of nanostructured biopolymer with tunable anisotropy, hierarchy, and functionality." *Next Materials* 2 (2024): 100140.

ABSTRACT OF THE DISSERTATION

Metamaterial for Enhanced Sensing and Power Management Application

By

Fan Ye

Doctor of Philosophy in Electrical and Computer Engineering

University of California, Irvine, 2024

Associate Professor Peter Tseng, Chair

This dissertation presents an innovative approach to multiparametric environmental and physiological signal monitoring using passive, wireless sensor networks. These networks, powered by a single radio frequency (RF) reader, utilize tunable relay coils and flexible RF sensors to spectrometrically co-monitor multiple chemical, physical, and biomechanical parameters, such as temperature, pressure, pH, nutrient levels, and joint angles, with a single readout. By integrating RF biosensors targeting key minerals like calcium and magnesium within a split-ring resonator architecture, the system enables the co-monitoring of multiple ions, ideal for precision nutrition applications. Additionally, textile-embedded magneto-inductive loops are introduced to monitor joint angles during dynamic movements, offering a robust solution for biomechanical assessment without interfering with natural motion or suffering from material fatigue. These advancements offer a scalable, durable, and adaptable solution for health monitoring, rehabilitation, and environmental sensing, overcoming traditional limitations of complex setups and sensor wear.

Chapter 1

Introduction

Wearable electronics, also known as wearable technology or wearables, refers to electronic devices or technologies that are designed to be worn on the body. These devices are seamlessly integrated into clothing, accessories, or even directly attached to the human body. Wearable electronics have gained significant popularity in recent years due to their potential to enhance our lives in various domains. They offer a wide range of functionalities, including health and fitness tracking, communication, entertainment, and even augmented reality experiences. From smartwatches and fitness bands to smart glasses and embedded sensors, wearable electronics have the capacity to collect and analyze data, provide real-time feedback, and offer personalized experiences. Their portability and continuous connectivity make them an integral part of the rapidly growing field of the Internet of Things (IoT). As technology advances, the potential applications of wearable electronics continue to expand, holding promise for revolutionizing healthcare, sports, fashion, and many other aspects of our daily lives.

In healthcare, monitoring nutrients is essential. Among nutrients, salts play an important role in electrolyte balance, nerve signal transmission[29], muscle contraction, and pH

regulation[70, 2, 66]in biological functions[42]. For example, sodium[38, 9], calcium, and magnesium[73, 75, 12, 74] are essential electrolytes that help maintain the balance of fluids in and out of cells[4], ensuring proper cell function and overall fluid balance in the body[34, 45], generating action potentials that allow communication between nerve cells[79, 59], enabling muscle contractions[49, 89] reflexes, and other physiological responses. Particularly, either excessive or insufficient intake of the divalent ions calcium or magnesium can have significant consequences for long-term bone health, immune function, or hormonal regulation. Too much calcium can lead to hypercalcemia[16, 95], which causes nausea[64], constipation, kidney stones[78, 6], and, in severe cases, impaired kidney function and heart rhythm disturbances. Imbalanced magnesium may cause muscle weakness and cramps[82], cardiovascular issues[90], mood disturbances[10], and more. Therefore, it is essential to maintain a balanced diet that includes an adequate intake of essential ions to support overall health and well-being. There remains an important need (for either personalized health or epidemiological purposes) for improved methods for tracking ions/minerals in foods and during consumption—this is particularly true for in personalized settings.

Many ion-detecting/modalities have been developed [77, 52] that are in use across a variety of different fields. Optical approaches, often in the form of commercial ion assay kits, can be used for single-use testing. [17, 30] Such techniques may have issues with sensitivity and measurements are easily confounded by unwanted light. For continuous quantitative measurements, ion-selective electrodes (ISE) are widely used. Such sensors are stable over long periods, can be reused[62, 28], are relatively low-cost, and exhibit high repeatability[88, 104]. Such electrodes are fundamentally formed from ion-selective membranes—these are composed of polymer membranes (often polyvinyl chloride, PVC) embedded with ionophores that selectively target specific ions for measurement. Many different ionophores have been developed targeting a wide variety of ions, including the key ions found in food. Conformal ISE-based sensors are either liquid-contact ISE or solid-contact ISE. Functioning on the potentiometric principle, ISEs gauge alterations in electrical potential (voltage) across the

electrode membrane upon interaction with the targeted ion. Both such electrodes have drift issues and require continuous recalibration[22, 33]. A drawback of liquid-contact electrodes lies in their relatively large size and intricate structures. Encompassing sensing components, battery parts, and wiring connections cannot be particularly tiny and flexible[24, 27, 25, 106]. This hinders seamless integration into user-friendly wearable devices. Furthermore, both ISE electrode subtypes require direct wiring to a printed circuit board (PCB), often leading to some contact in the test environment with solder, microelectronics, or metal wiring (particularly in compact formats). This may potentially pollute the solution or lead to measurement error.

Besides nutrients, monitoring human movement is crucial in healthcare. The analysis of human movement primarily focuses on the torso’s dynamics and its interaction with joint movements. The ability to track these movements smoothly and continuously in real-time is highly valuable across numerous fields, including rehabilitative medicine[40, 7, 101, 97], sports science[85], ergonomic research, entertainment and gaming[103], security, and virtual/augmented reality technologies[61, 100].

Current techniques for monitoring joint movements employ a variety of technologies, each with its own benefits but also limitations that hinder their ability to capture motion comprehensively. Nonwearable systems like optical cameras, whether using retroreflective markers[31, 39] or operating markerless[87, 32], are limited to lab environments due to their need for a clear line of sight. Electromagnetic methods utilizing antennas for backscattering[1], radar[76], and Wi-Fi networks[58] can identify physical activities from afar but are mainly suitable for indoor use and often prioritize activity classification over detailed motion analysis, such as bending or rotating. Wearable solutions, including time-of-flight technologies that use ultrawideband or ultrasonic signals[65] to measure signal travel times, are constrained by their size and potential injury risks. Inertial measurement units[63] offer greater freedom from lab settings and user comfort but face challenges with sensor drift and are

power-hungry. Bend sensors[44, 77], are placed directly across joints to detect changes in resistance due to strain, limit movement, and have a short operational life due to wear. Additionally, the use of microelectronics with soldered connections in some devices makes them prone to movement-induced damage, reducing their durability and design flexibility.

The realm of smart textiles[91, 92, 57, 56, 35] represents a shift toward more integrated and user-friendly wearable technologies. Innovations in this area particularly benefit from the concept of “strongly coupled magnetic resonance” between flexible inductors[3, 72]. The applications of these structures extend from serving as passive sensor nodes[71, 26, 27, 25] to enabling wireless power transmission[86, 41, 102, 36, 37]. There has been a magnetic inductive approach[68, 80, 105] that uses wireless power transfer efficiency to monitor joint angles. They position loop antennas longitudinally along the joint, mitigating the issues associated with lateral placement across the joint. However, this approach has not yet been tried on the human body and necessitates the use of multiple ports because of its primary concern on transmission efficiency (insertion loss S21).

Readout is another crucial aspect of monitoring. Spectrometric readout is widely used in modern science, where electromagnetic (EM) radiation of varying frequencies can be used to probe matter in its varying forms (whether simple or complex). Spectral signatures that manifest from such EM interactions are used as an important identification tool in chemistry, physics, and biomedicine[69, 5, 19, 14]. A major characteristic of this readout is its data-rich nature, which enables a significant amount of information to be extracted in a single measurement. This manifests from the differential response of matter to varying EM wavelengths that may span X-rays, UV–vis, terahertz, and radio frequency (RF)[8, 21, 54, 46]. Some of the most widely utilized methods include a material-under-test that is excited directly by a broad spectrum of radiation—examples include Fourier transform infrared/UV–vis[13, 67] and mass spectrometry[20, 50, 84], wherein characteristic peaks over a broad spectrum yield rich, multiparametric data on the material-under-test.

Modern processing techniques enable a more focused cousin of this approach, wherein matter is organized into structures that interact with radiation in a directed way, such as to exhibit resonance phenomena[48, 98, 99]. This approach can be used to create more selective/sensitive sensors that are typically intended to measure a single value[53, 93, 51, 83]. A common example of this is RF sensors, wherein conductive traces are patterned so as to resonate when excited by RF waves[43, 71, 18, 55]. Such an approach has been adapted to build sensors and biosensors sensitive to a variety of chemophysical signals, such as pressure[11, 37], temperature[96, 60, 23], glucose[47, 24], salinity[81, 15], nutrients[25, 94], and more. Despite the emerging versatility of this approach, RF sensor readout is still highly limited, as typically only a single sensor is assessed at a time, and the technique is not stable to mechanical noise because the readout coil and sensor alignment are typically not fixed.

I firstly study a form of programmable RF spectrometry, wherein a single readout of RF spectra can be used to assess a wide variety of desired chemophysical signals from the environment. This is in contrast to the standard readout of multiparametric signals where individual sensing formats require unique signal conditioning circuitry and/or processing. Here, RF waves interact with multilayers of electronics-free patterned, wirelessly coupled elements that can be engineered to various length scales, to deform or attach around surfaces, and tuned to controlled reactivity to chemical or physical signals. This is broad expansion of more basic iterations of this technique that monitors arrays of pressure sensors via planar readout coils, or the radiation of an array of temperature sensors. In our study, RF signal is first mediated by passive intermediate relay coils that are wireless and electrically disconnected from other elements. This can transfer signal over intermediate distances and can be fused onto textiles or conform over surfaces. These relays are then wirelessly coupled to RF sensors with tunable environmental reactivity—demonstrated herein including pressure, temperature, salinity, and nutrients (sugars/salts/fats). This then forms a multiparametric network composed exclusively of passive material architectures. Beyond the fully passive/wireless readout of multiparametric signals, this approach is significantly more ro-

bust in comparison to traditional RF readout—this is because intermediate coil to RF sensor alignment can readily remain fixed through design. In general, any capacitive or resistive sensor type may be integrated with our technique, as these readily build into RF sensors such as those we show herein. As proof-of-concepts, I demonstrate multiparametric, chemo-physical readouts from wireless wristbands and SmartCups that are infused with multilayers of interacting, flexible/reactive wireless elements.

Then I demonstrate passive wireless nutrient monitoring networks capable of decoupling multiple ions from complex food biofluids. The core sensors are built from split-ring resonators previously utilized by our group for a variety of applications in physical and biochemical sensing. Here, these are integrated with ion-selective membranes to enable the measurement of specific ions. These radiofrequency (RF) sensors are fully passive and wireless while being composed exclusively of food-safe polymer and metal foil. Sensors are compact and the lack of wiring or circuitry is a major advantage for food measurement. Furthermore, RF sensors are probed nondestructively at high frequencies (100 s of MHz), in contrast to wired ISEs that are measured at DC/low-frequencies—such low-frequency open circuit voltage measurements are invariably prone to drift because faradaic currents can cause unwanted transformations in the reference and working electrodes. This may further be caused by imbalances in the circuit electronics wherein minor DC current flows that further lead to signal drift or membrane modulation. My wireless sensors are not connected to any circuitry and are not subject to faradaic currents. My resonator construct has additional advantages over previously studied RF ion sensors—those utilize planar electrodes with significant fringing fields that will significantly reduce sensor selectivity. Such fringing fields do not penetrate through the ion-selective membrane (ISM) and interact with non-specific ions outside of the intended sensing region.

My RF sensors are built into wireless sensor arrays that enable multimineral measurement. In practice, many ISMs do not exhibit perfect selectivity and will partially chelate/absorb

similar ions. This is particularly true for divalent ions such as Magnesium and Calcium, whose ISM have moderate selectivity against each other and can confound each other's measurement. I develop strategies to both co-measure multiple ion RF sensors (individually tuned to measure different ions), and mathematically-extract individual ion concentrations. Robust sensor array readout is enabled by codesign of an optimized readout coil that aligns to the array. For example, in a cup, the RF sensors can be arrayed within the cup itself, while the readout coil conforms on the outside of the cup to yield repeatable measurement (in such a scenario only the RF sensors contact food). Here I optimize the readout coil geometry to boost RF signal strength and enhance relevant sensor signal/sensitivity. Notably this approach adapts to diverse food ware and containers encountered by food, ranging from flat ones (plates) to more complex shapes like curved objects. As a practical demonstration, I measure the calcium and magnesium composition of milk fortified to different divalent ion contents—this is accomplished with passive wireless sensing networks integrated into a cup. My approach resolves one of the traditional major limitations of RF sensors, being single target monitoring and imperfect selectivity of that sensor.

I lastly present a pair of strongly coupled magnetic resonators for joint angle monitoring that relate the coupling coefficient and reflection (return loss S_{11}) at the reader port, thereby reducing the number of required ports to a single one. The operating principle can be better understood using Faraday's law of induction. Strong coupling between two resonators alters their resonant frequencies due to mutual energy exchange, resulting in the creation of two new frequencies higher and one lower than the original and can be captured by reader port in return loss. The pair of coils can be directly applied onto clothing or skin, eliminating the need for microelectronics and batteries to be worn on the body. The system's readout is achieved through a portable/wearable mini vector network analyzer (miniVNA), which removes the necessity for bulky equipment. This method utilizes adaptable magneto-inductive loops strategically positioned on each side of a joint, promoting an unrestricted range of motion and minimizing the risk of mechanical failure due to frequent material flexing.

These loops are designed to be planar and flexible, maintaining stable spectral behavior close to human tissue by integrating a lumped capacitor to counteract the skin's stray capacitance. Initial angle calibration was conducted with the coils alone and subsequently confirmed with tests on the human body, before finally synthesizing multijoint monitoring networks. A rule-based method that relies on measured angles was used to classify a variety of movements.

Chapter 2

Passive Sensor System Codesign Methodology

2.1 Tx+Sensor

Let $Z_r = R_r + j\omega L_r + \frac{1}{j\omega C_r}$, $Z_s = R_s + j\omega L_s + \frac{1}{j\omega C_s}$, from the definition of S_{11} :

$$S_{11} = \frac{Z_{in} - Z_0}{Z_{in} + Z_0} \quad (2.1)$$

$$Z_{in} = (Z_r - j\omega M) + j\omega M \parallel (Z_s - j\omega M) \quad (2.2)$$

Put Z_{in} in:

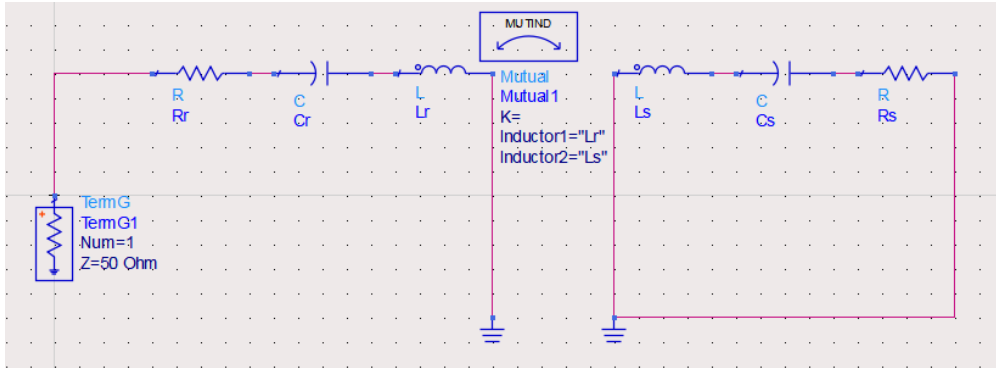


Figure 2.1: The equivalent circuit of the reader and RF sensor system. The mutual inductance(M) may take different values depending on the alignment between the reader and sensor.

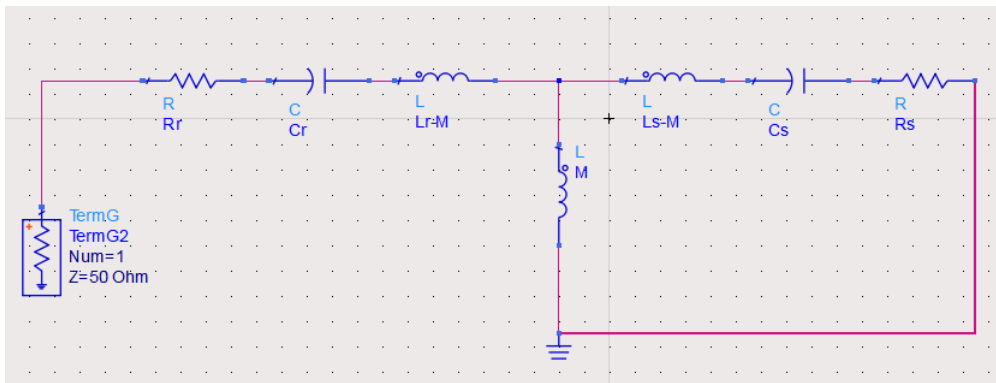


Figure 2.2: Modifying the equivalent circuit of the reader and RF sensor system using the T model

$$S_{11} = \frac{Z_r - j\omega M + \frac{j\omega M(Z_s - j\omega M)}{Z_s} - Z_0}{Z_r - j\omega M + \frac{j\omega M(Z_s - j\omega M)}{Z_s} + Z_0} \quad (2.3)$$

$$= \frac{Z_r + \frac{\omega^2 M^2}{Z_s} - Z_0}{Z_r + \frac{\omega^2 M^2}{Z_s} + Z_0} \quad (2.4)$$

Set the real part of $Z_r + \frac{\omega^2 M^2}{Z_s}$ to x , the imaginary part to y , rewrite S_{11} as:

$$S_{11} = \frac{(x - Z_0) + yi}{(x + Z_0) + yi} \quad (2.5)$$

$$|S_{11}| = \frac{\sqrt{(x - Z_0)^2 + y^2}}{\sqrt{(x + Z_0)^2 + y^2}} \quad (2.6)$$

Assume For minimum magnitude of S_{11} , it is equivalent to minimize $|S_{11}|^2$:

$$f(x, y) = \frac{(x - Z_0)^2 + y^2}{(x + Z_0)^2 + y^2} \quad (2.7)$$

Take partial derivative on the imaginary part:

$$\frac{\partial f(x, y)}{\partial y} = \frac{2y[(x + Z_0)^2 + y^2 - (x - Z_0)^2 - y^2]}{[(x + Z_0)^2 + y^2]^2} \quad (2.8)$$

$$= \frac{8yxZ_0}{[(x + Z_0)^2 + y^2]^2} \quad (2.9)$$

Since $x > 0$, $Z_0 > 0$:

$$f(x, y)_{min} = f(x, 0) \quad (2.10)$$

$$\frac{\partial f(x, y)}{\partial x} = \frac{2(x - Z_0)[(x + Z_0)^2 + y^2] - 2(x + Z_0)[(x - Z_0)^2 + y^2]}{[(x + Z_0)^2 + y^2]^2} \quad (2.11)$$

$$= \frac{4Z_0(x^2 - Z_0^2 - y^2)}{[(x + Z_0)^2 + y^2]^2} \quad (2.12)$$

Since $y = 0$, $Z_0 > 0$:

$$f(x, y)_{min} = f(Z_0, 0) \quad (2.13)$$

This result indicates that a resonant Tx is preferred, where the Tx is designed to resonate at the frequency of the sensor, providing increased sensitivity: $w_r = w_s = w_0$, $\text{img}(Z_r(w_0)) = \text{img}(Z_s(w_0)) = 0$.

Consider Tx and sensor resonance in initial S_{11} :

$$S_{11}(w_0) = \frac{\frac{w_0^2 M^2}{R_s} - Z_0}{\frac{w_0^2 M^2}{R_s} + Z_0} \quad (2.14)$$

Tune k match $\frac{w_0^2 M^2}{R_s}$ to Z_0 , as $M = k\sqrt{L_r L_s}$.

For Tx resonates at a frequency that is different from the sensor, in the phasor form we have:

$$Z_r + \frac{w^2 M^2}{Z_s} = |Z_r|e^{j\theta_r} + \frac{w^2 M^2}{|Z_s|e^{j\theta_s}} = |Z_r|e^{j\theta_r} + \frac{w^2 M^2}{|Z_s|^2} |Z_s|e^{j(-\theta_s)} \quad (2.15)$$

In this case, we first tune k and L_r to match $\text{real}(\frac{w_0^2 M^2}{R_s})$ to Z_0 , then tune C_r to match Z_r to $\text{img}(\frac{w_0^2 M^2}{R_s})$. w_0 will fall out of range between w_r and w_s in order to cancel out the imaginary

part.

2.2 Tx+Multi-Sensor

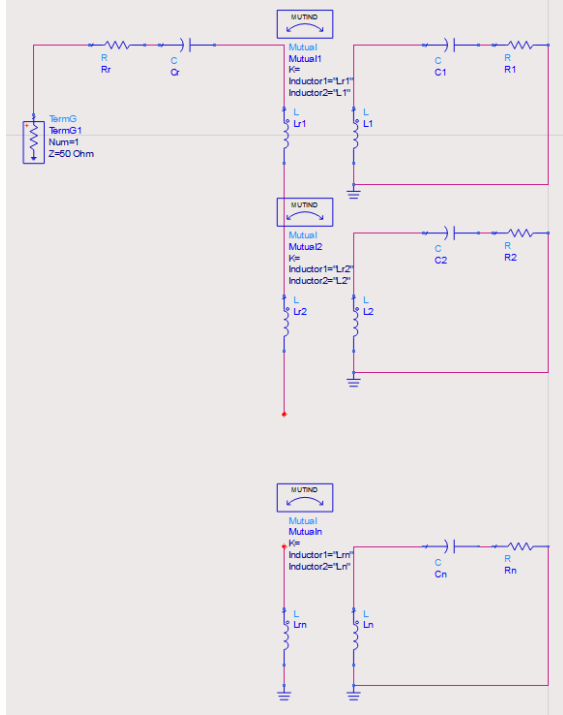


Figure 2.3: The equivalent circuit of the larger reader and RF sensor system. The mutual inductance(M) may take different values depending on the alignment between the reader and sensor.

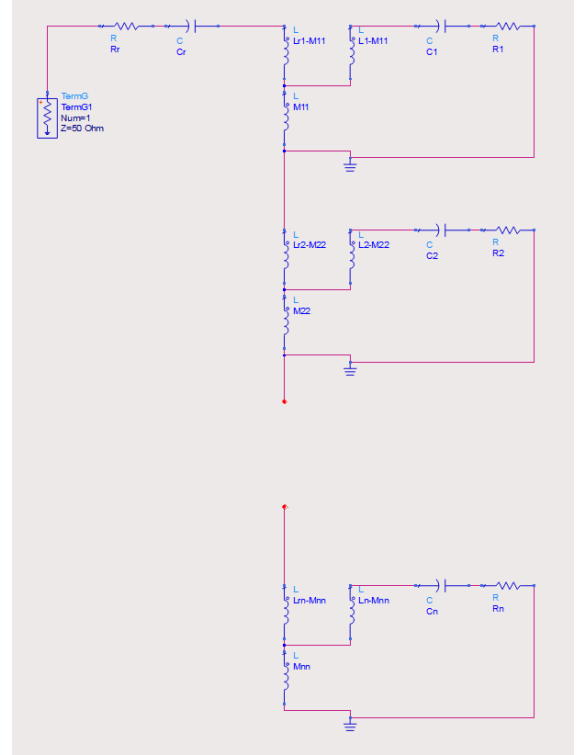


Figure 2.4: Modifying the equivalent circuit of the larger reader and RF sensor system using the T model

Let $Z_r = R_r + j\omega L_r + \frac{1}{j\omega C_r}$, ($L_r = L_{r1} + L_{r2} + L_{r3} + \dots + L_{rn}$); $Z_n = R_n + j\omega L_n + \frac{1}{j\omega C_n}$, ($n = 1, 2, 3, \dots$). from the definition of S_{11} :

$$S_{11} = \frac{Z_{in} - Z_0}{Z_{in} + Z_0} \quad (2.16)$$

$$Z_{in} = (Z_r - jwM_{11} - \dots - jwM_{nn}) + jwM_{11}|| (Z_1 - jwM_{11}) + \dots + jwM_{nn}|| (Z_n - jwM_{nn}) \quad (2.17)$$

Put Z_{in} in:

$$S_{11} = \frac{Z_r + \sum_{i=1}^n \frac{w^2 M_{ii}^2}{Z_i} - Z_0}{Z_r + \sum_{i=1}^n \frac{w^2 M_{ii}^2}{Z_i} + Z_0} \quad (2.18)$$

Still consider the imaginary part:

$$Z_r + \sum_{i=1}^n \frac{w^2 M_{ii}^2}{Z_i} = |Z_r| e^{j\theta_r} + \sum_{i=1}^n \frac{w^2 M_{ii}^2}{|Z_i| e^{j\theta_i}} = |Z_r| e^{j\theta_r} + \sum_{i=1}^n \frac{w^2 M_{ii}^2}{|Z_i|^2} |Z_i| e^{j(-\theta_i)} \quad (2.19)$$

During the frequency sweep, the term $\frac{w^2 M_{ii}^2}{|Z_i|^2}$ will continue to dominate the imaginary part when $w \rightarrow w_i$, generating local minimum on $|S_{11}|$ spectrum.

For multiple ports in Figure 1.6:

$$S_{11} = \frac{(Z_{r1} + \frac{w^2 M_{11}^2}{Z_1}) || (Z_{r2} + \frac{w^2 M_{22}^2}{Z_2}) || \dots || (Z_{rn} + \frac{w^2 M_{nn}^2}{Z_n}) - Z_0}{(Z_{r1} + \frac{w^2 M_{11}^2}{Z_1}) || (Z_{r2} + \frac{w^2 M_{22}^2}{Z_2}) || \dots || (Z_{rn} + \frac{w^2 M_{nn}^2}{Z_n}) + Z_0} \quad (2.20)$$

Let $R_s = \text{real}(Z_{ri} + \frac{w^2 M_{ii}^2}{Z_i}) \approx \text{real}(\frac{w^2 M_{ii}^2}{Z_i})$, $X_s = \text{img}(Z_{ri} + \frac{w^2 M_{ii}^2}{Z_i})$. $i = 1, 2, 3, \dots, n$. Consider series to parallel conversion:

$$Z_p = \frac{jR_p X_p}{R_p + jX_p} = \frac{R_p X_p^2}{R_p^2 - X_p^2} + j \frac{R_p^2 X_p}{R_p^2 - X_p^2} \quad (2.21)$$

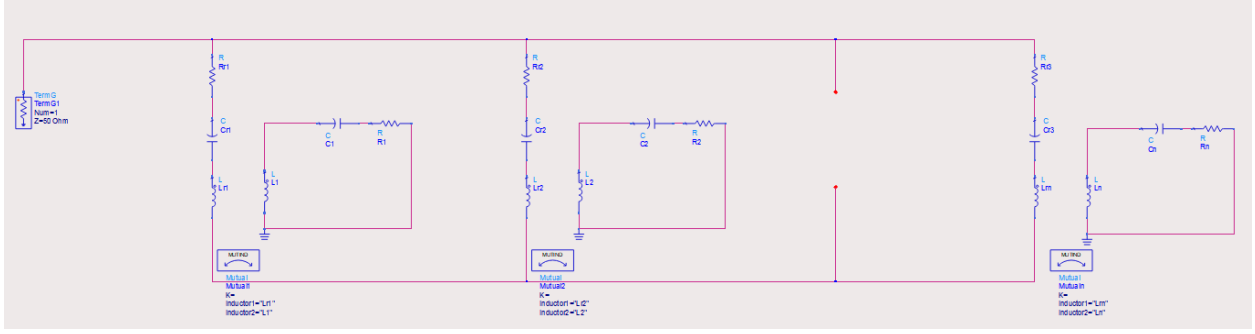


Figure 2.5: The equivalent circuit of the multi-port reader and RF sensor system. The mutual inductance(M) may take different values depending on the alignment between the reader and sensor.

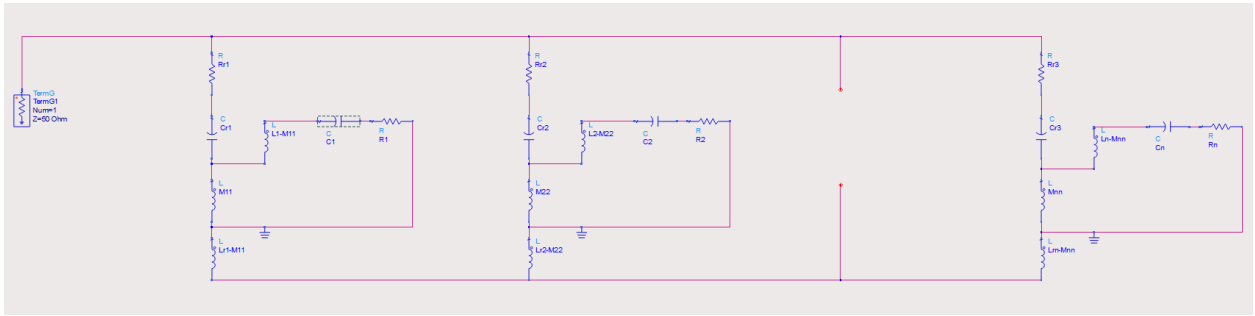


Figure 2.6: Modifying the equivalent circuit of the multi-port reader and RF sensor system using the T model

We have:

$$\frac{R_p X_p^2}{R_p^2 - X_p^2} = R_s \quad (2.22)$$

$$\frac{R_p^2 X_p}{R_p^2 - X_p^2} = X_s \quad (2.23)$$

Solve for R_p and X_p :

$$X_p = \frac{X_s^2 - R_s^2}{X_s} \quad (2.24)$$

$$R_p = \frac{X_s^2 - R_s^2}{R_s} \quad (2.25)$$

Rewrite S_{11} :

$$S_{11} = \frac{R_{p1}||R_{p2}||\dots||R_{pn} + X_{p1}||X_{p2}||\dots||X_{pn} - Z_0}{R_{p1}||R_{p2}||\dots||R_{pn} + X_{p1}||X_{p2}||\dots||X_{pn} + Z_0} \quad (2.26)$$

The optimization of $|S_{11}|$ will be varying L_{r1} to match $R_{p1}||R_{p2}||\dots||R_{pn}$ to Z_0 and $X_{p1}||X_{p2}||\dots||X_{pn}$ to 0. These two conditions usually cannot be satisfied simultaneously, but by proper adjustment of L_{r1} , a local minimum can always be found near the resonance frequency of a single sensor.

2.3 Tx+IR+Sensors

Let $Z_r = R_r + j\omega L_r + \frac{1}{j\omega C_r}$, $Z_{IR} = R_{IR} + j\omega L_{IR1} + j\omega L_{IR2} + \frac{1}{j\omega C_{IR}}$, $Z_s = R_s + j\omega L_s + \frac{1}{j\omega C_s}$.

From the definition of S_{11} :

$$S_{11} = \frac{Z_{in} - Z_0}{Z_{in} + Z_0} \quad (2.27)$$

$$Z_{in} = Z_r - j\omega M_1 + (((Z_{IR} - j\omega M_2) + j\omega M_2)|(Z_s - j\omega M_2)) - j\omega M_1) || j\omega M_1 \quad (2.28)$$

$$= Z_r - j\omega M_1 + (Z_{IR} + \frac{\omega^2 M_2^2}{Z_s} - j\omega M_1) || j\omega M_1 \quad (2.29)$$

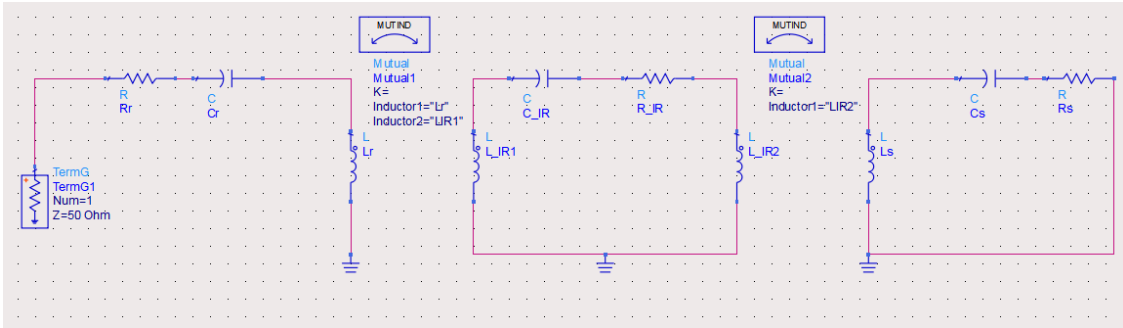


Figure 2.7: The equivalent circuit of the reader, intermediate relay, and RF sensor system. The mutual inductance(M) may take different values depending on the alignment between the reader, intermediate relay, and sensor.

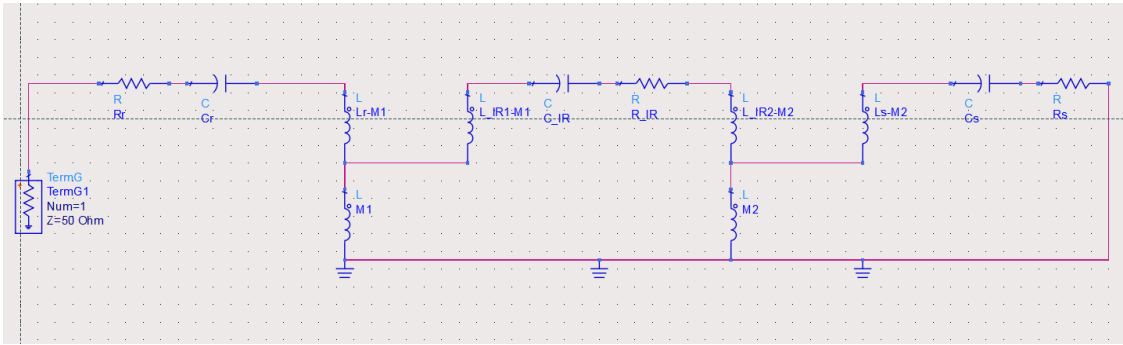


Figure 2.8: Modifying the equivalent circuit of the reader, intermediate relay, and RF sensor system using the T model

Set $Z_{IR} + \frac{w^2 M_2^2}{Z_s}$ as Z_{tot} :

$$Z_{in} = Z_r + \frac{w^2 M_1^2}{Z_{tot}} \quad (2.30)$$

$$S_{11} = \frac{Z_r + \frac{w^2 M_1^2}{Z_{tot}} - Z_0}{Z_r + \frac{w^2 M_1^2}{Z_{tot}} + Z_0} \quad (2.31)$$

From a similar logic in section 1.1 and section 1.2, $|S_{11}|$ will display an obvious minimum value after proper tune of Z_r , Z_{IR} , and the configuration between them. We can also expand this general case to n intermediate relay case.

2.4 Tx+Resonate Coil Pair

We have exact same S_{11} expressions as (eq 2.31), but $Z_{tot} = Z_s + \frac{w^2 M_2^2}{Z_s}$ since sensor 1 and sensor 2 are identical. We ignore the coupling between the reader and sensor 2 for simplicity. For numerical analysis, we set component values in Figure 1.8, and the $|S_{11}|$ map is plotted from eq.1.31. By varying the coupling coefficient between sensor 1 and sensor 2, the minimum value of $|S_{11}|$ splits. The separation between two local minimum values can be used to monitor the change in the relative position of two sensors.

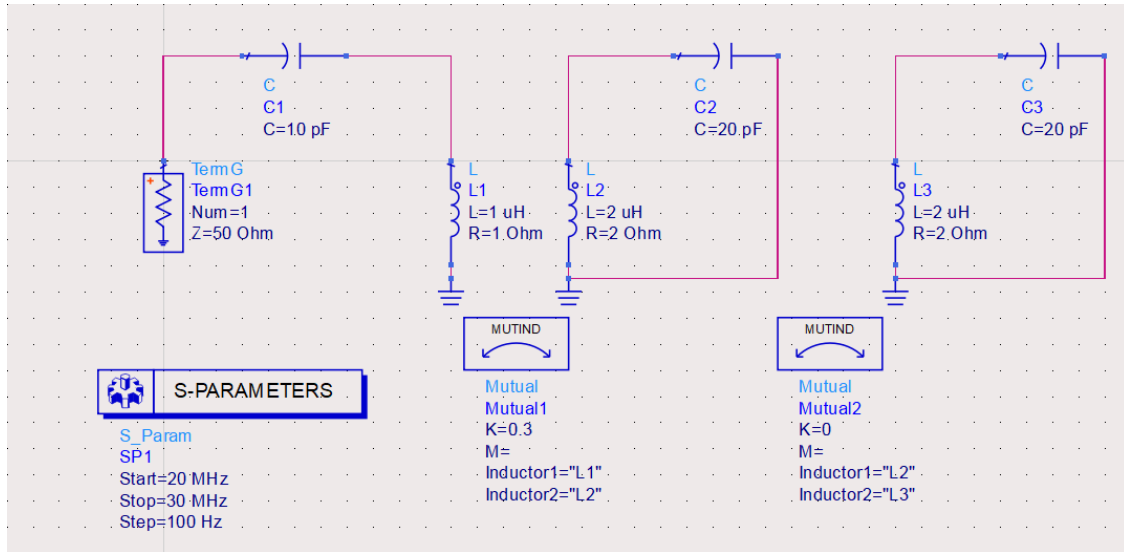


Figure 2.9: The equivalent circuit of the reader, sensor1 and sensor 2. The mutual inductance(M) may take different values depending on the alignment between the reader and sensors.

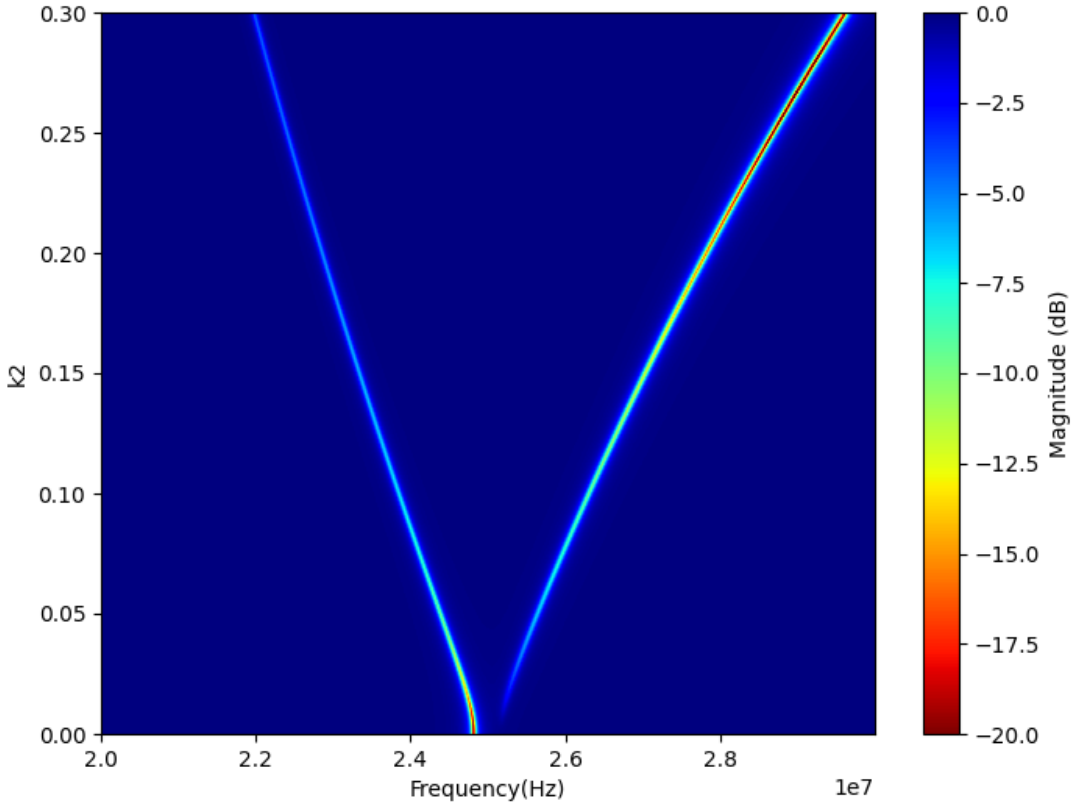


Figure 2.10: Plot $|S_{11}|$ through eq 2.31 with components' value from Figure 1.9

Chapter 3

Passive and Wireless, Ion-Selective Sensor Arrays for Multimineral Comonitoring of Food

3.1 Sensing Methodology and Properties

Our basic RF sensor is formed from two broadside-coupled, reverse-facing split ring resonators that are interceded by an ion-selective membrane (Figure 3.1). This can be probed wirelessly through nearfield coupling, wherein its spectral properties can be linked to RF sensor environment. The basic behavior of our resonator is illustrated through a straightforward series RLC circuit analogy, where the resonant frequency is estimated by: $f = 1/2\pi\sqrt{LC}$. This further exhibits a quality factor, Q , relating to the energy stored and dissipated by the resonator. This leads to a characteristic resonant peak when probed wirelessly. In this scenario, a simple reader coil (an inductor that is connected to a Vector Network Analyzer-VNA) is aligned to the sensor. This VNA can then read the reader-sensor network parameters

(such as reflection coefficient, S_{11}). Considering the symmetric nature of the circuit shown in Figure 3.4b, we write the reflection coefficient for one sensor for simplicity:

$$S_{11} = \frac{Z_r + \frac{\omega^2 M^2}{Z_s} - Z_0}{Z_r + \frac{\omega^2 M^2}{Z_s} + Z_0} \quad (3.1)$$

where Z_r is the impedance of the reader, Z_s is the impedance of ISM, Z_0 is the port impedance, M is the mutual inductance between ISM and the reader. The capacitance (and thus impedance) of the resonator links to the interlayer region in between the split ring electrodes membrane. This exhibits a complex relative permittivity expressed as $\epsilon = \epsilon_1 - j\epsilon_2$. In many RF sensors, there is minimal dissipation within the capacitance of the structure and ϵ_2 can be ignored. The presence of charged molecules, however, significantly increases this ϵ_2 parameter, creating an additional loss term in the capacitance. Such charges effectively reduce the Q of the resonator, impacting the magnitude of the resonant peak.

In the case of resonators with ion-selective membrane interlayers, the capacitance is subject to variations driven by changes in the ion-selective membrane's chelation/absorption of ions from the environment. This modulates with the concentration of ions in the environment, as higher ion absorption enhances the conductivity of the membrane (as ions oscillate in RF electric fields). This increases the overall loss tangent in the interlayer and increases the losses of the resonator (reducing Q). Thus, the primary mode of sensing in these structures is through measuring the magnitude response (or S_{11}) of the sensor. A particular advantage of our resonator is the focusing of electric fields to in between the split-ring electrodes, making the sensor signal link exclusively to the absorption characteristics of the ISM (Figure 3.1e). The minimal fringing fields of the parallel electrode plates reduce environmental interference and improve the selectivity of the sensor. Our sensors are designed to resonate between 100 to 600 MHz, meaning the interlayer is effectively probed at these high frequencies. Such RF

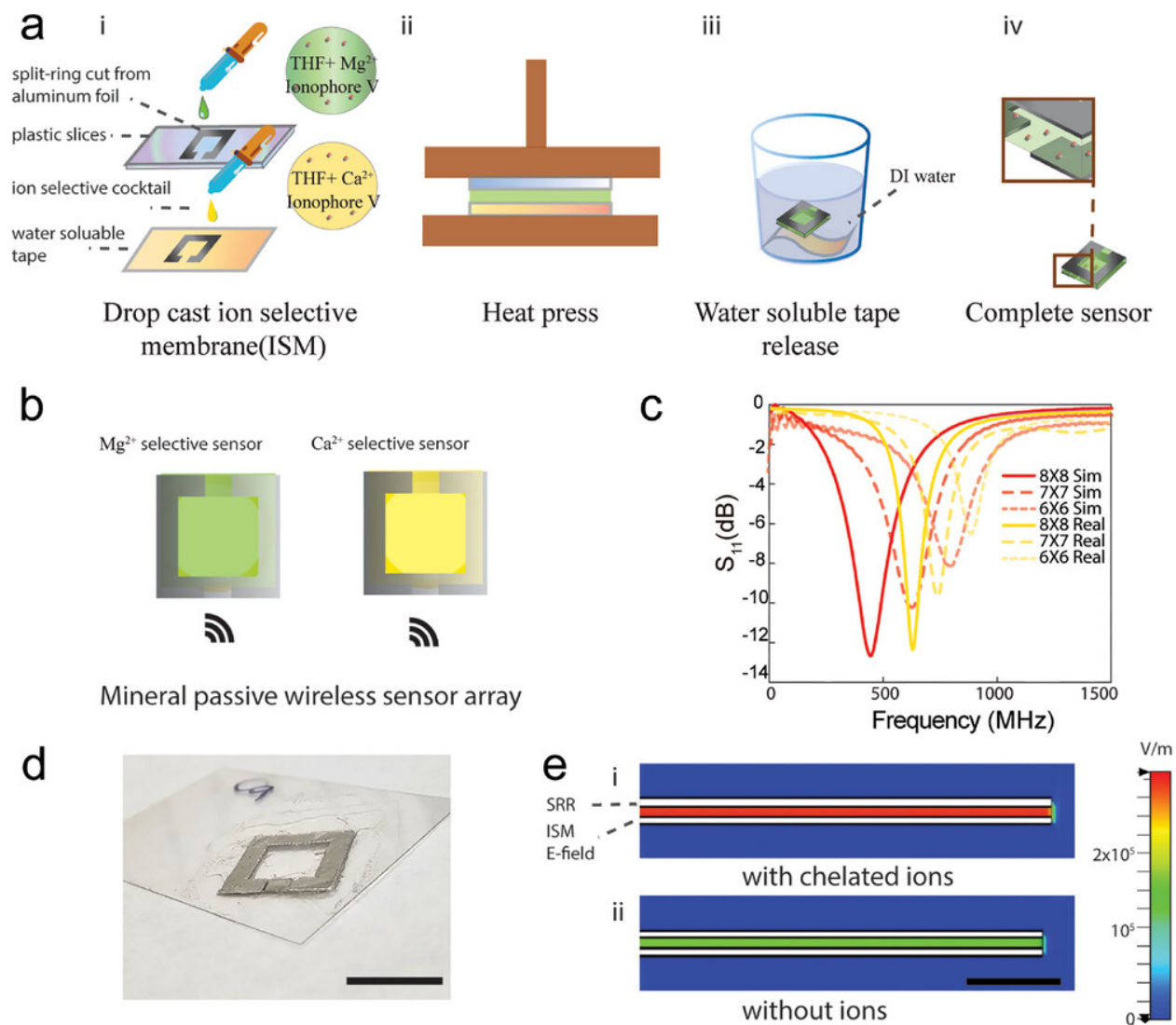


Figure 3.1: Passive wireless ion-selective RF sensor arrays. a) RF ion-selective sensor fabrication process. b) RF sensors are arrayed to monitor multiple minerals. Herein we integrate calcium and magnesium ISM into respective sensors to facilitate measurement of these two key divalent ions. c) Simulated and measured spectral response of ion-selective RF sensors sized to different area footprints. Size measurement is in centimeters. d) Image of fabricated resonator. Scale bar is 8 cm. e) Simulation results of the sensor with i) and without ii) ions. The electric field is exclusively focused in between split rings to maximize sensor selectivity. With ion presence, the resonator absorbs more energy and exhibits larger electric field intensity. Scale bar is 1 mm

measurement minimizes any potentially destructive low-frequency faradaic currents.

We utilized the CST Microwave Studio frequency domain solver to simulate the behavior of an ion-selective RF sensor (Figure S1, Supporting Information). We set the relative permittivity of the interlayer at 10. While PVC has a relative permittivity of 3 to 4, ISM contains around 20% water which increases the effective relative permittivity. The interlayer conductivity is set at 0.1 S m, and interlayer thickness can be varied (from 50 to 80 μm in increments of 10 μm). Similarly, we can enlarge the dimensions (side length from 8 to 5 mm) of the split ring, leading to a rise in simulated eigenfrequency. A summary of simulated resonator characteristics is exhibited in Figure S2 (Supporting Information), showing how the spectral behavior of the resonator modulates with changing design parameters. Last, a comparison between the spectral behavior of simulated and actual RF sensors is shown in Figure 3.1c, both showing similar trends in resonant frequency and S11 magnitude as the size of the resonator is spanned. A key is the tunability of sensor resonant frequency. This will be utilized later as multiple sensors must be co-measured and cannot overlap in spectral response.

3.2 Fabrication and Basic Response of Ion-Selective RF Sensors

To synthesize ion-selective RF sensors (Figure 3.1), aluminum foil is first cut via a vinyl cutter to form split rings of various sizes as designed using L-edit. The split rings are 8 cm. Split rings are subsequently attached to either a plastic coverslip (the substrate) or water-soluble tape. Ion-selective polymer cocktail is deposited onto each split ring and allowed to evaporate. By estimating the volume of solid components within the solvent solution, we can estimate the thickness of the interlayer. Thicker membranes can be created through

repeated deposition and drying of cocktails. Here, we repeat this process five times to obtain a 30 μm thickness of ISM. To improve repeatability, split rings are carefully aligned under a microscope with assistance from a micromanipulator, and the volume of the ISM cocktail is carefully weighed for each replication to be consistent. Multiple sensors are made (ISM deposition, split-ring alignment) in parallel using this same cocktail to ensure homogeneity in membrane thickness across multiple sensors. The split rings are lastly heat-pressed together, before being submerged in water for water-soluble tape dissolution. At this point, the sensors are ready for use. One advantage of this technique is that the active ion-selective membrane region is protected by the electrode stack. Our cocktail is composed of PVC polymer, ionophore, and the solvent tetrahydrofuran (THF). Here we focused on implementing ionophores targeting calcium (Ca) and magnesium (Mg), respectively. These divalent ions are both important in food and additionally can be challenging to co-measure. Their targeting ionophores will weakly/moderately chelate other divalent ions in addition to their primary target. Upon solvent evaporation and final sensor completion, the construct is formed exclusively from aluminum foil and PVC polymer materials, both of which can be synthesized in food-safe formats. The response of our sensor comes from the position of the sensor and antenna.

We first performed a series of experiments to characterize the basic properties of our sensor, such as selectivity, hysteresis, and longevity. These studies were performed on benchtops, where sensors are affixed to a Petri dish and the readout coil is stably aligned below the dish. We first tested the sensitivity and selectivity of the Ca and Mg RF sensors, respectively. Here, our key sensor output is simply the peak magnitude S11 of the readout coil. Relevant targeted ions are first introduced (either Ca or Mg), followed by the same concentration of sodium (Na). This step is repeated, with increasing concentration doses (this is typical of experiments with voltaic ISE as well). Both Ca and Mg ionophores are highly selective against Na. As expected, our RF sensors exhibited high selectivity against Na (Figure 3.2), and the introduction of Na only minimally modulates the sensor peak S11. The sensitivity

($\log K$) is less than 2, which is similar to voltaic ISM sensor counterparts. As sodium is common in many foods, this trait is an important one. The actual spectral response of our sensors in all these concentrations is shown in Figures S3a and S4a (Supporting Information), indicating minimal magnitude response in Na as opposed to targeted ions. We next tested the hysteresis of both the sensitivity and selectivity of our sensor. This is one way to test the stability of our measurement and whether it impacts baseline sensor behavior. Sensor response to repeated steps up high concentrations of salts is shown in Figure 3.2c,g. Importantly the response returns to baseline after repeated exposures and returns to the original state (deionized water), and additionally appears unimpacted by larger salt concentrations (spectral responses shown in Figure S5, Supporting Information). We lastly tested the 10-day response of sensor sensitivity (Figure 3.2d,h). After 10 d, the sensor exhibits similar step response and selectivity as in day 1. Open-circuit voltage measurements typically exhibit drift over time during voltaic measurement (that necessitates recalibration after storage or repeated usage), and our results indicate that the high-frequency probing of ISM may potentially minimize transformations within the membrane. After all the testing experiments, we first rinsed the sensor with deionized water to clean it. Then, we immersed the sensor in the DI for 30 minutes. This process is repeated until the sensor response returns to its original behavior.

3.3 Ion-Selective RF Sensor Arrays

Although both Ca and Mg ion-selective RF sensors show a very high selectivity over sodium ions, this property is not as high as each other. This is because these ion-selective membranes exhibit some cross-reactivity with other divalent ions. We characterized the sensitivity and selectivity of our respective RF sensors to Ca and Mg (Figure 3.3). Calcium ion-selective RF sensors exhibit a noticeable unwanted response to Mg, and magnesium ion-selective RF

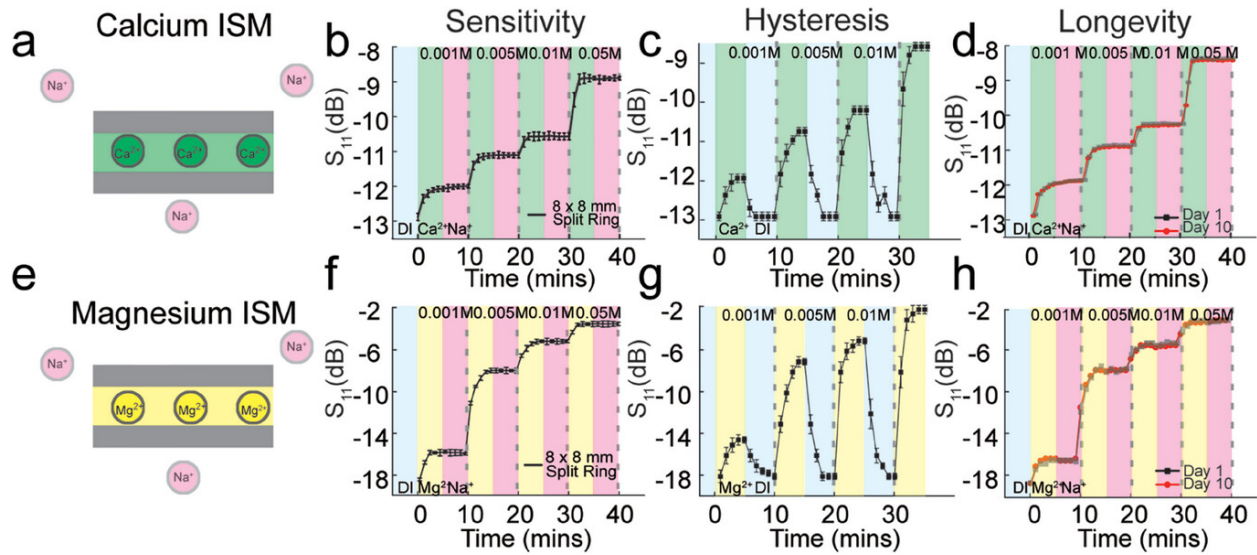


Figure 3.2: Ion-selective RF sensor performance parameters. a) Side-view schematic of calcium-selective RF sensor and membrane selectivity against sodium. b) Sensitivity and sodium selectivity of RF sensors ($N = 3$). c,d) Hysteresis and 10 d response of calcium-selective RF sensor. e) Side-view schematic of magnesium-selective RF sensor and membrane selectivity against sodium. f) Sensitivity and sodium selectivity of RF sensors ($N = 3$). g,h) Hysteresis and 10 d response of magnesium-selective RF sensor.

sensors exhibit an unwanted response to Ca (Figure 3.3b,e). The full spectral response of an example sensor is shown in Figures S3b and S4b, Supporting Information). These responses are indicative of the weaker selectivity of these sensors to other divalent ions as opposed to Na. This is currently a fundamental limit to present ionophores and limits the measurement accuracy of single sensors. The selectivity between Ca and Mg is around 2:1. The selectivity between Mg and Ca is around 3:2. This can be seen in the extracted sensitivity of sensors to respective molecules (Figure 3.3c,f).

To resolve this, we synthesized passive wireless sensor networks that can more accurately characterize the ionic content of environments. These are first composed of arrays of ion-selective RF sensors interacting with food (herein two sensors with Ca and Mg ion-selective membranes). Sensor responses can be combined with basic analytical techniques to better estimate individual ion concentration. These are secondly co-aligned with a custom, optimized readout coil that can flank on the other side of surfaces to enhance multisensor readout. The

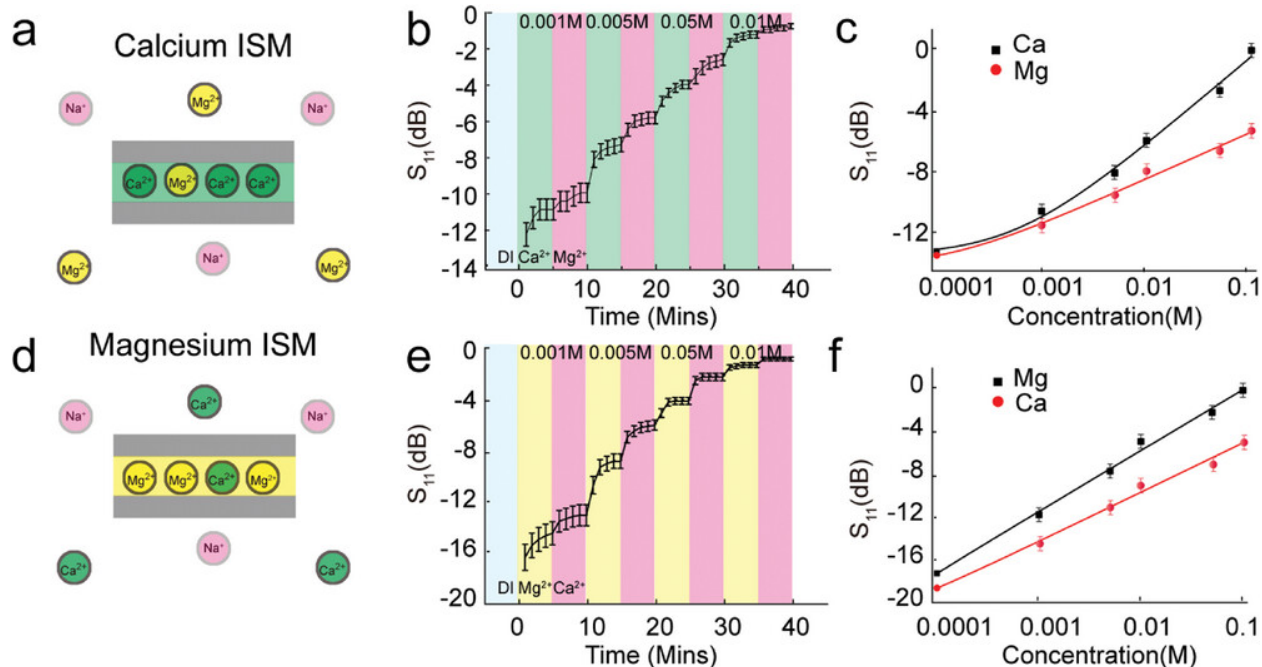


Figure 3.3: Ion-selective RF sensor characterization when in the presence of the divalent ion. a) Calcium ISM exhibits moderate selectivity against magnesium. b,c) Sensitivity and selectivity of calcium-selective RF sensor to calcium and magnesium in deionized water. $N = 3$. Curves can be fitted to individual sensor responses to describe its sensitivity to different ions. d) Magnesium ISM exhibits moderate selectivity against calcium. e,f) Sensitivity and selectivity of magnesium-selective RF sensor to magnesium and calcium in deionized water. $N = 3$. Like above, curves can be fitted to individual sensor responses to describe its sensitivity to different ions.

sensor array and RF coil can be fused onto a variety of surfaces or elements to form a stable passive wireless ion measurement network.

To extract concentrations from the two imperfect ion-selective RF sensors, we first characterize the sensitivity of respective sensors to each ion within the to-be-utilized biofluid (this may be water, milk, juice, etc.). We make a basic first-order assumption that our ion responses are additive, so we thus model the two-sensor array as a basic set of general equations:

$$S_{11} = A \ln[c(\text{calcium})] + B \ln[c(\text{magnesium})] + D \quad (3.2)$$

here the letter variables are those extracted from initial calibration within various biofluids. This system can be readily solved to estimate the calcium and magnesium within our biofluid.

Our array is measured using a coaligned, customized wireless readout coil. Here, these were vinyl-cut from conductive foil—note that this readout coil does not need to be touching food. For example, within a cup the sensors populate the interior side, however, the readout coil needs only be affixed to the outer side of the cup to allow the wireless nearfield coupling to the RF sensor array (Figure 3.4a). Such a strategy mechanically fixes the entire passive readout network, stabilizing readout and eliminating alignment headaches that may occur. Several engineering tasks must further be done to optimize sensor co-readout. Sensors should not either physically or spectrally overlap, for two sensors they should be oriented across from each other and their resonant frequency should be at minimum 100 MHz from each other. This can be done by changing the area footprint or interlayer thickness. Here we chose to simply synthesize two different thicknesses of the ISM interlayers to modulate the two sensor resonant frequencies. We further optimized the readout antenna by focusing the magnetic field to each respective sensor, effectively giving each sensor a local inductive loop to probe it

(Figure 3.1a). These loops should be oriented in parallel to minimize interference (wideband circuit model shown in Figure S6, Supporting Information). This circuit model indicates that increasing the input signal frequency leads to an uneven surface current distribution and subsequent uneven magnetic field. This unevenness can cause the reader antenna to fail in coupling with the sensors at certain points. The parallel setup offers a significant advantage by avoiding local minima in the sensing area, thus improving magnetic field delivery to individual split-ring resonators. Further enhancement of the antenna’s performance involves fine-tuning the input impedance by adjusting the conductor traces’ lengths (transmission lines) and geometries (transmitting inductance) and incorporating a lumped surface-mount capacitor. These adjustments allow precise tuning of the reader’s resonance, ensuring that the energy delivered to the sensors is balanced and results in clear, distinct peaks for each sensor in the S11 spectrum. Technically, this leads to two local minima in input impedances on the Smith chart (Figure S7, Supporting Information) at the reader port. A simulation of the magnetic fields generated by our technique is shown in Figure S8 (Supporting Information), indicating the focusing of magnetic fields to respective sensor regions. We expect that this approach can generalize to increasing array size (or count). Readout coils optimized in such a manner exhibit significantly lower noise (Figure S9, Supporting Information).

We demonstrate the functionality of such networks we sought to measure the ion content of milk fortified to varying levels of magnesium and calcium (Figure S10, Supporting Information). We expect that most different food matrices will not impact sensor response—this includes starches and fiber (long-chained carbohydrates) or protein (long-chained polypeptides). These large, hydrophilic molecules do not interact with the ISM. We have found that the presence of oil/fat can have a slight impact on sensor sensitivity (such as in milk). We believe this is because the hydrophobic small molecules can interact with the surface of the ISM, thus modulating ion penetration slightly. We thus used milk as a complex food biofluid on which to test our approach. Fortified milk was formed by diluting milk to different levels and introducing Mg and Ca to various concentrations. The sensitivity of our sensors to

respective ions in these environments was first calibrated (Figure 3.4c,d). From here the system of equations describing the behavior of our sensor array in milk is derived. We then modulated the concentration of Ca and Mg to 10 random concentration groupings. As expected, the sensor array (and our simple numerical solution) achieves significantly higher accuracy than single sensor measurement (Figure 3.4e). A table delineating our percent error is shown in Figure S11 (Supporting Information), indicating that we typically achieve within 10% and below the accuracy of the actual concentration of both calcium and magnesium. Such measurements were extracted directly from a single co-measurement using our optimized readout coil (Figure S12, Supporting Information). The presence of fat (whether in whole or diluted milk) had a similar effect on performance in our tested solutions. It is possible there would be a dose-response curve at sufficiently low concentrations of milk, potentially at the level of skim milk (.5%) and below.

Food environments can be biofouling, and we expect that our sensors will need to be cleaned after repeated exposure to such environments. In general, we expect our washing procedures to be similar for ion-selective electrodes, which similarly go through potential biofouling environments. Such ISM will last for 2 years and will need to be cleaned by rinsing under running water, light blotting, or wiping away from the active area of the sensor and soaking while not in use. Our sensors remained usable after 3 to 4 DI water wash steps, although we expect sensor response could drift after significant exposure to biofouling environments without thorough cleaning.

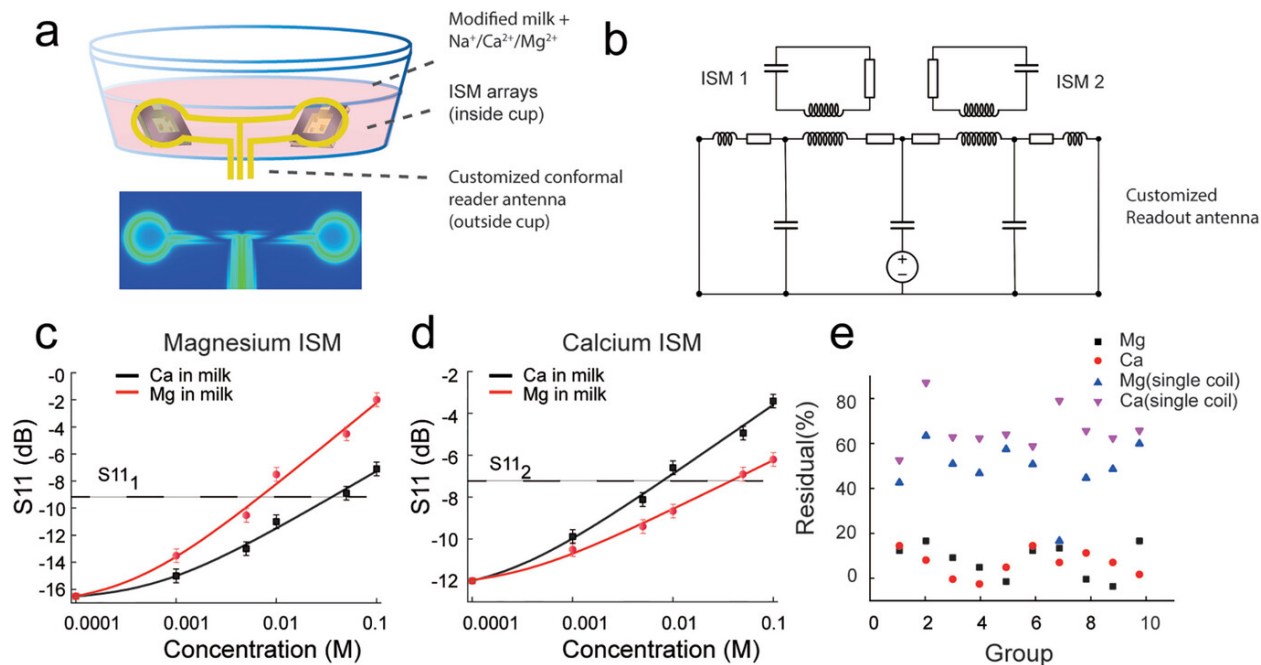


Figure 3.4: Optimized, food ware-integrated passive wireless network to measure divalent ions. a) Ion-selective RF sensors are oriented inside the cup. Outside the cup is a cup-conforming, custom readout coil that attaches and aligns adjacent to the sensor array. This readout coil exhibits nearfield magnetic hotspots that match sensor positioning. b) Circuit diagram of readout coil and sensor array. c,d) Respective RF sensor sensitivities calibrated in diluted milk. e) Reduced percent error measurement in a random grouping of magnesium/calcium concentrations enabled by our sensor measurement and basic numerical extraction approach.

Chapter 4

Programmable Multiwavelength Radio Frequency Spectrometry of Chemophysical Environments through an Adaptable Network of Flexible and Environmentally Responsive, Passive Wireless Elements

Our approach is composed of three types of RF elements that are wirelessly coupled to form the complete circuit, as shown in Figure 4.4.1Ai. First are readout coils that form the initial inductive link into our passive sensor network, and that is probed via a direct wired connection to a reader (such readers include tabletop or wearable vector network analyzer (VNA)). The inductive readout coil can be designed as a one-port circular coil for S_{11} or a two-port microstrip patch line for S_{21} spectral response readout (Figure S1,

Supporting Information). Herein, we utilized either a 25 mm diameter circular readout coil (feed line length 35 mm) or a U-shaped microstrip patch line (25 and 35 mm traces) that are selectively integrated with FR-4 substrate (fabrication of which is discussed in Supporting Information). Second is an intermediate relay (IR) coil that is untethered from all other elements. This is wirelessly coupled with the readout coil, transferring the EM fields to subsequent sensors along its path length or through designed inductive terminals. This IR plays an important role in the structure—in our manifestation, it is synthesized on a flexible substrate and subsequently fused onto curved surfaces or textiles. This allows RF signals to transmit over materials/substrates relevant to our daily lives and can be tuned to transfer signals over arbitrary distances. Beyond facilitating information from localized sensing nodes, these enhance the mechanical robustness of the sensing network. Sensor alignment to the intermediate coil is simple to maintain due to the flexible/routing nature of the IR—as will be seen this helps stabilize the spectral readout to misalignment between the readout coil and network. This adds significant flexibility to the final passive sensor network. We demonstrate various practical manifestations wherein the IR coil is embedded alongside a cup to enable a SmartCup to monitor nutrients in food (Figure 4.4.1B), or fused on a textile to facilitate readout of a wristband from across the arm (Figure 4.4.1C, and S2, Supporting Information).

Third and lastly are passive and wireless RF sensors with individually tunable mechanical or chemical reactivity. These sensors are passive resistance–inductance–capacitance structures that are built to modulate with environmental signals. Herein, we utilize broadside coupled, split ring resonating architectures that have been previously characterized by our group. One key aspect of our strategy is the utilization of interlayer-RF sensor design schemes such as those we have previously demonstrated.[30, 32, 35] Modulation of the lumped resistance of a sensor changes the magnitude, while modulation of the lumped capacitance shifts the resonant frequency of its spectral response. Individual sensors are built with specialized materials (both within and around the sensing architecture) and thus rendered selectively

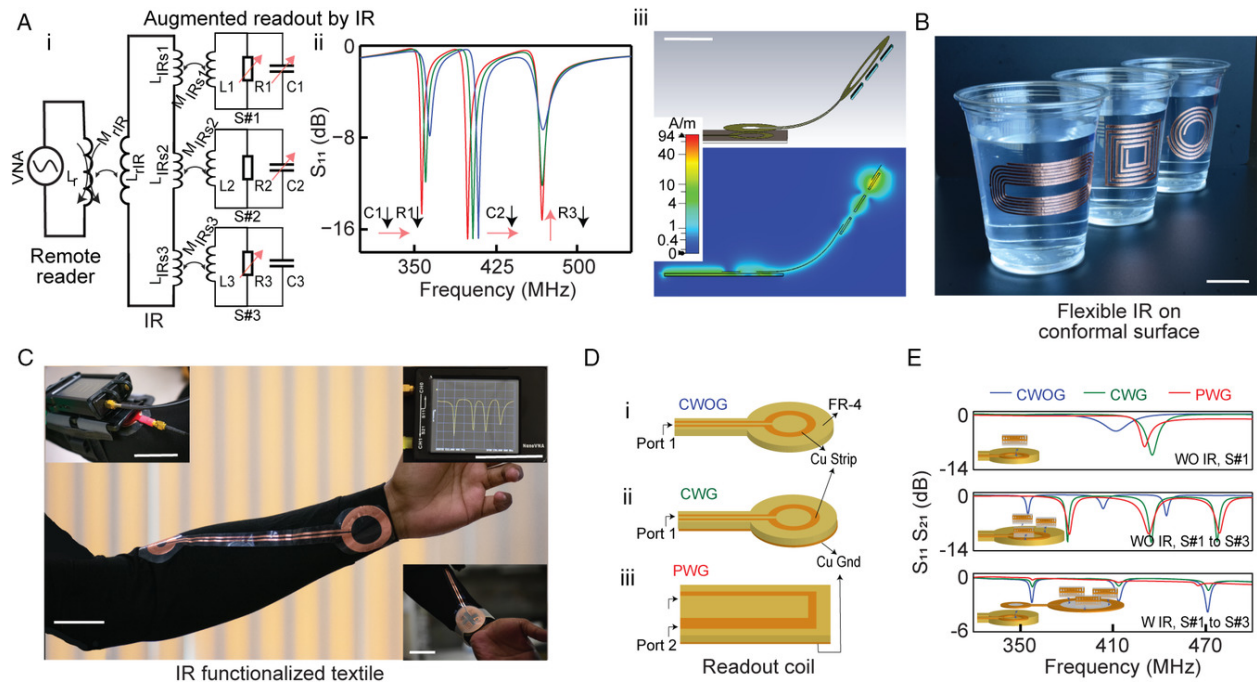


Figure 4.1: Programmable multiwavelength RF spectrometry of the chemophysical environment. A) A network composed of multilayers of passive (zero-electronic) elements enables single readout monitoring of complex signals. (i) Circuit diagram of reader wirelessly coupled to an IR, in turn wirelessly coupled to tunable RF sensors, (ii) RF simulation of the spectral readout where sensor 1 is perturbed by both R1 and C1, sensor 2 is perturbed only in C2, and sensor 3 is perturbed only in R3, (iii) geometry used in finite element method (top) and corresponding magnetic field distribution showing magnetic coupling between elements. B) Flexible IR is integrated into the outer surface of cups. C) IR-integrated smart textile to facilitate multiparametric wristband readout. Insets are the placement of the wristband and direct readout from wearable NanoVNA. D) Readout antenna structures studied herein (i) circular without ground (CWO), (ii) circular with ground (CWG), and (iii) planar with ground (PWG). E) Spectral readout from various network configurations: single sensor without IR (diameter of the readout coil loop is 25 mm), multiple sensors without IR (diameter of the readout coil loop is 50 mm), and multiple sensors with IR (diameter of the IR loop is 50 mm). The standard vertical distance between the readout coil/IR loop and sensors is 0.5 mm. For multisensor readout, the orientation of the sensors remains constant. Scale bars are 5 cm.

sensitive to metrics such as glucose, sugars, salts, fats, pressure, temperature, and more.[25, 30, 32, 35, 44] Importantly, these structures are readily tuned to respond/resonate at different wavelengths and thus occupy individual frequency bands during spectral readout. This occurs by simply varying the thickness of the interlayer. This allows us to readily tune any sensor of a set square area (size footprint) to hit variable operating frequencies. Thus, for our sensors (0.5–1 cm wide) we could readily tune response to occupy various desired bands for different environmental responses. These sensors are oriented along the IR coil, and whose resonance can be probed through the intermediate relay signal.

The final, versatile structure is a fully passive sensor network (requiring zero electronics) that can monitor complex chemophysical signals in a single readout. Figure 4.4.1Aii shows the RF simulation of the readout of three sensors (numbered S1, S2, and S3, respectively). Here, both C1 and R1 of S1, only C2 of S2, and only R3 of S3 are perturbed. Enlargement of R3 decreases the signal magnitude, and reduction in C2 increases the resonant frequency, while reduction in both R1 and C1 decreases the signal magnitude and increases the resonant frequency, respectively. These modulations map exclusively to the spectral band occupied by individual sensors. Figure 4.4.1Aiii shows a finite element simulation of the magnetic fields within a sample network. This field distribution displays the multiple layers of wireless magnetic coupling between the readout coil and sensors via the IR. This system exhibits additional power loss in comparison to traditional RF sensor readout due to the additional wireless couplings—specifically the coupling between the readout coil and IR, and the coupling between IR and sensors. The effect of this interceding coil can be seen in the reduced magnitude S11 response of the multi-coil network as opposed to the direct readout of sensors (this is for the same input dBm to both configurations). The impact of the lower S11 is that shifts in the magnitude and frequency of resonant sensors may become more difficult to resolve. A higher power may be used to increase the total S11 response, and thus improve the readout of very low-sensitivity sensors, but there is an upper limit to the total power that may be applied in wearable, or close-to-body applications. Thus, in networks using an

IR require moderate-to-high sensitivity sensors are be required in near-body environments. However, we note that this type of moderate-to-high sensitivity is not difficult, as all our demonstrated sensors herein are easily probed/measured with -5 dBm (300 mW), which is standard for many wearable applications in the near field.

In this article, we studied three readout antennas for targeting different applications: circular without ground plane (CWOG), circular with ground plane (CWG), and patch with ground plane (PWG), as shown in Figure 4.4.1D. The CWOG is a circular loop readout coil pasted on the FR-4 substrate which has one port connected to the VNA, whereas the CWG is the same readout coil but the other side of the FR-4 substrate has a conductive ground plane. PWG is a microstrip patch line that has two ports connected to the VNA, and the common ground pin is shorted via the connection with the ground plane on the other side of the FR-4 substrate. A detailed layout is presented in Figure S1, Supporting Information. Sensors are of variations of interlayer RF structures, but our fundamental structure was a 15 mm-wide, 3.25-turn spiral square trilayer structure (Figure S3, Supporting Information). This structure is modulated in several ways to broadly tune the sensor to different resonant frequencies while retaining the same footprint: via modification of the coil turn number or interlayer thickness. Figure 4.4.1E compares the spectral readout of single and multiple sensors when probed by various readout antennas, with and without an IR interceded within the structure. We additionally studied the effect of different vertical distances between the antenna and sensors, which modulates the spectral response due to changing coupling coefficient (Figure S4, Supporting Information). Finite-difference time-domain simulation was additionally performed to model the behavior of the sensor and readout coil resonant spectra and to map the EM field distribution (Figure S5, Supporting Information). It can be seen that the grounded structures exhibit a larger EM field close to the readout coil; however, this decays more rapidly than the ungrounded structure as we move away from the coil. Both E and H fields are higher with CWG than CWOG at a 3 mm separation between the readout coil and sensor—this matches the higher Q measured with CWG. We additionally simulated

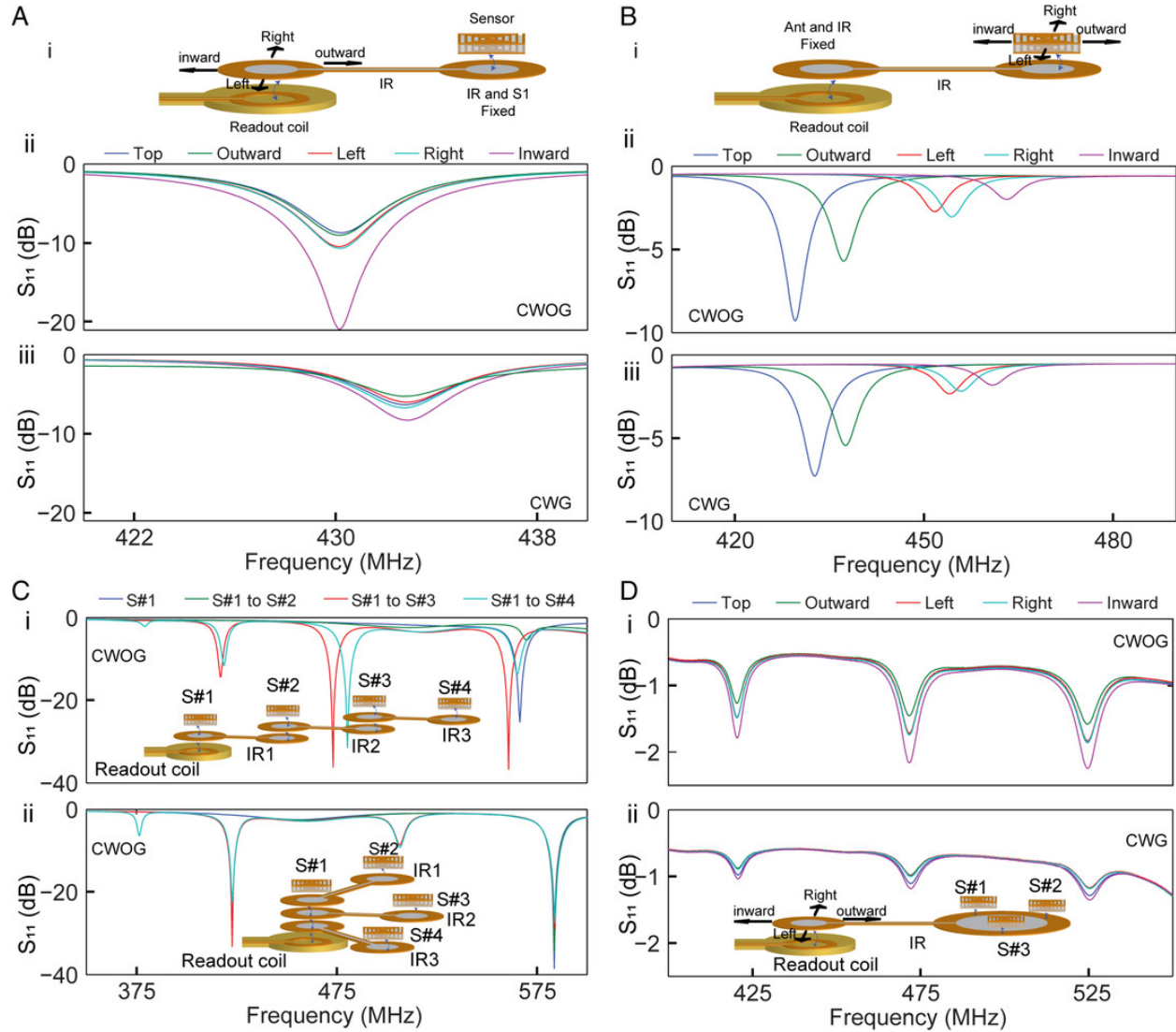


Figure 4.2: Augmented readout via network coupling through an IR. A) Effect of the alignment between readout antenna and IR when IR and sensor orientation is fixed: (i) schematic presentation of the orientation of the antenna, IR, and sensor, network S₁₁ response by (ii) CWOG, and (iii) CWG. B) Effect of the alignment between IR and sensor while antenna and IR are fixed: (i) schematic of network orientation, network S₁₁ response by (ii) CWOG and (iii) CWG. C) Readout of multiple sensors through multiple IR. Network S₁₁ response during (i) series and (ii) parallel extension. Insets are the network orientation. D) Readout of multiple sensors by IR. Effect of the alignment between readout antenna and IR when IR and sensor orientations are fixed: network S₁₁ response by (i) CWOG (ii) CWG. Inset is the network orientation.

the effect of bending on sensor readout (Figure S6, Supporting Information). As shown in the following figure, the impact of one or two large folds is a minor shift in the measured resonant frequency/magnitude of the sensor. This shift is around ± 0.7 MHz (0.2% shift) in frequency and 2 dB in magnitude. This puts a limitation on the sensitivity of our sensors in the case of dynamic bending environments, which must possess a sensitivity higher than this “noise” to be measured properly. Figure 4.4.1E (middle) shows the readout of three sensors each tuned to different resonant frequencies. Interestingly, the CWOG coil structure exhibits a higher amplitude than the grounded structures in the presence of an IR (Figure 4.4.1E bottom). The slower decay of EM field away from the ungrounded structure improves signal transmission through this intermediate structure, which must be wirelessly coupled over a set distance. This knowledge can be utilized to optimize network readout and design depending on the presence of an IR, and the coupling distance of the various elements of the network. This will be seen in the measurement/implementation of wireless wristbands and “smart” cups later in this study. As an additional note, in all such scenarios, the EM field is seen to be strongly confined between the individual sensor and the readout coil, which means there is negligible magnetic cross-coupling among nearby sensors.

We next explored various network orientations involving the presence of the IR. First, we studied the effect of the alignment of the readout antenna and an IR30/30 (30 mm loop diameter for both readout coil and sensor coupling) while the IR and sensor placement is fixed (Figure 4.4.2A, exploded view of the schematic in Figure S7, Supporting Information). As can be seen, the translational alignment between the antenna and the IR has little to no effect on the resonant frequency. This stability in the spectral response importantly means that sensors that exhibit shifts in resonant frequency due to environmental perturbations remain measurable even if the readout coil is misaligned from the sensor network. This enhanced mechanical stability is important because this readout coil-to-network alignment is often not fixed because the reader is commonly brought up to the network and subsequently removed after readout. Note that sensors that shift in magnitude are still measurable given

their sensitivity is larger than the magnitude shifts induced by perturbation (this can be tuned by targeting less sensitive regions to align/realign the readout coil to the network). Next, we fixed the antenna and IR30/30 placement and studied the effect of the IR and sensor alignment (Figure 4.4.2B). As expected, we observed that sensor coupling is strongly dependent on the orientation of the sensor with the IR, which can result in shifts to both the resonant frequency and the signal amplitude. This means that this IR–sensor alignment should remain fixed throughout the measurement. We note that this is the primary purpose of the IR, which is flexible/conformable and can permanently route the signal to desired regions as required by the application. This instability is similar to when the readout coil and sensors exhibit mechanical translations without the presence of an IR (Figure S8, Supporting Information). Multiple IR may additionally be coupled to the readout coil via series or parallel extension (Figure 4.4.2C), where differing numbers of sensors are added to the network. In series extension, sensors placed further in the network modulate the spectral response due to sensor cross-coupling. This disappears for parallel extension, where additional sensors can be added without modulating the measured resonant frequency of previous sensors (in this scenario sensors are coupled only to the IR but not each other). Multisensor networks are additionally stable to mechanical translation (Figure 4.4.2D). These results broadly indicate that IR interceded sensor networks can provide stabilized readout given a wide variety of scenarios. One limitation of using the IR is elongating the ends will lead to a reduction in signal amplitude (and thus limits the practical sensitivity of the measurement). There is a very direct trade-off, where very long distances will require either higher sensitivity sensors or higher input power to resolve measurements.

We performed additional simulations to illustrate the effect of increased length on the measured S11 (Figure S9, Supporting Information). At 50 cm the measured S11 of sensors does decrease in comparison to shorter distances, as various sensors will exhibit magnitude shifts of 1–4 dB at this distance (higher frequency sensors are more robust to increased distances). From these findings, it appears as though at very long distances sensors can be pushed to

higher operating frequencies to maintain similar readout sensitivity. In general, we have found even -1 dB of amplitude response to be sufficient for the proper measurement of our particular RF sensors.[36]

In such a passive network, a large number of sensors can potentially be accommodated, the limits of which can be assessed through measurement of the cross-coupling among sensors. We initially tested sensor positional coupling as they were arrayed in increasing numbers above readout coils (Figure 4.4.3A). This type of coupling is not as important as sensor measurement coupling, the results of which will follow. Seven sensors were placed initially on the readout coil (the minimum physical distance of the adjacent sensors is 2 mm) and sensors were removed one by one. We found that for ungrounded readout coils, the removal of sensors from a dense network could lead to small shifts in the measured resonant frequency of remaining sensors on the network (Figure 4.4.3Aii). On the other hand, for CWG, there is no effect due to the removal of sensors from seven to one, as shown in Figure 4.4.3Aiii (full data on these experiments is shown in Figure S10, Supporting Information, for CWOG and in Figure S11 for CWG, Supporting Information). In addition, as shown earlier, the measured sensor amplitude is stronger for CWG during this direct multisensor readout. This type of coupling effect due to sensor placement was additionally tested with an IR (Figure S12, Supporting Information), and shows a positional effect for both CWOG and CWG in agreement with this observed effect. This implies that given a dynamic sensor network wherein sensors may be picked and placed, grounded RF elements will simplify sensor measurement due to minimal positional coupling. One fundamental limitation of such a system is the maximum number of sensors that can be measured. For low-cost (wearable) VNA systems that accurately measure response up to 1.5 GHz, the primary limitation comes in the bandwidth that sensors occupy. Generally, approximately 100 MHz band per sensor is more than sufficient to properly assay individual sensors (smaller bandwidth is required for more sensors that shift less in frequency with perturbation). For low-cost systems, with sensors that occupy 100 MHz, we can assume that we can accommodate around 15 RF

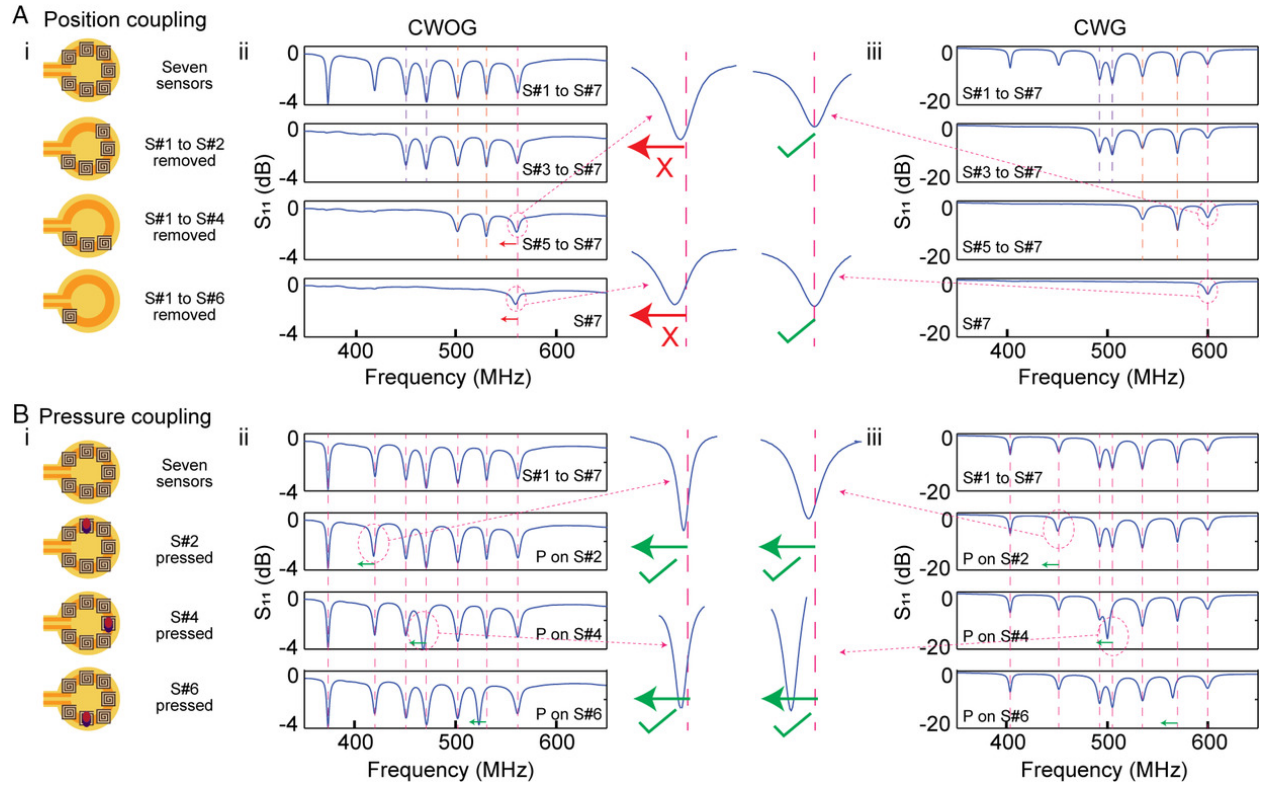


Figure 4.3: Cross-coupling effect among sensors. A) Effect of positional coupling between sensors: (i) schematic presentation of sensor array orientation during experiment, and S₁₁ response from sensors with (ii) CWOG and (iii) CWG readout antennas. In between is a blow-up plot highlighting the shift or lack of shift in resonant frequency due to coupling. B) Effect of sensimetric coupling between sensors (applied pressure): (i) schematic presentation of applying stimuli to various sensors, and S₁₁ response from sensors with (ii) CWOG and (iii) CWG readout antennas. In between is a blow-up plot highlighting the shift in resonant frequency of the spectral peak linked to respective sensors. No other peak exhibits a shift.

sensors.

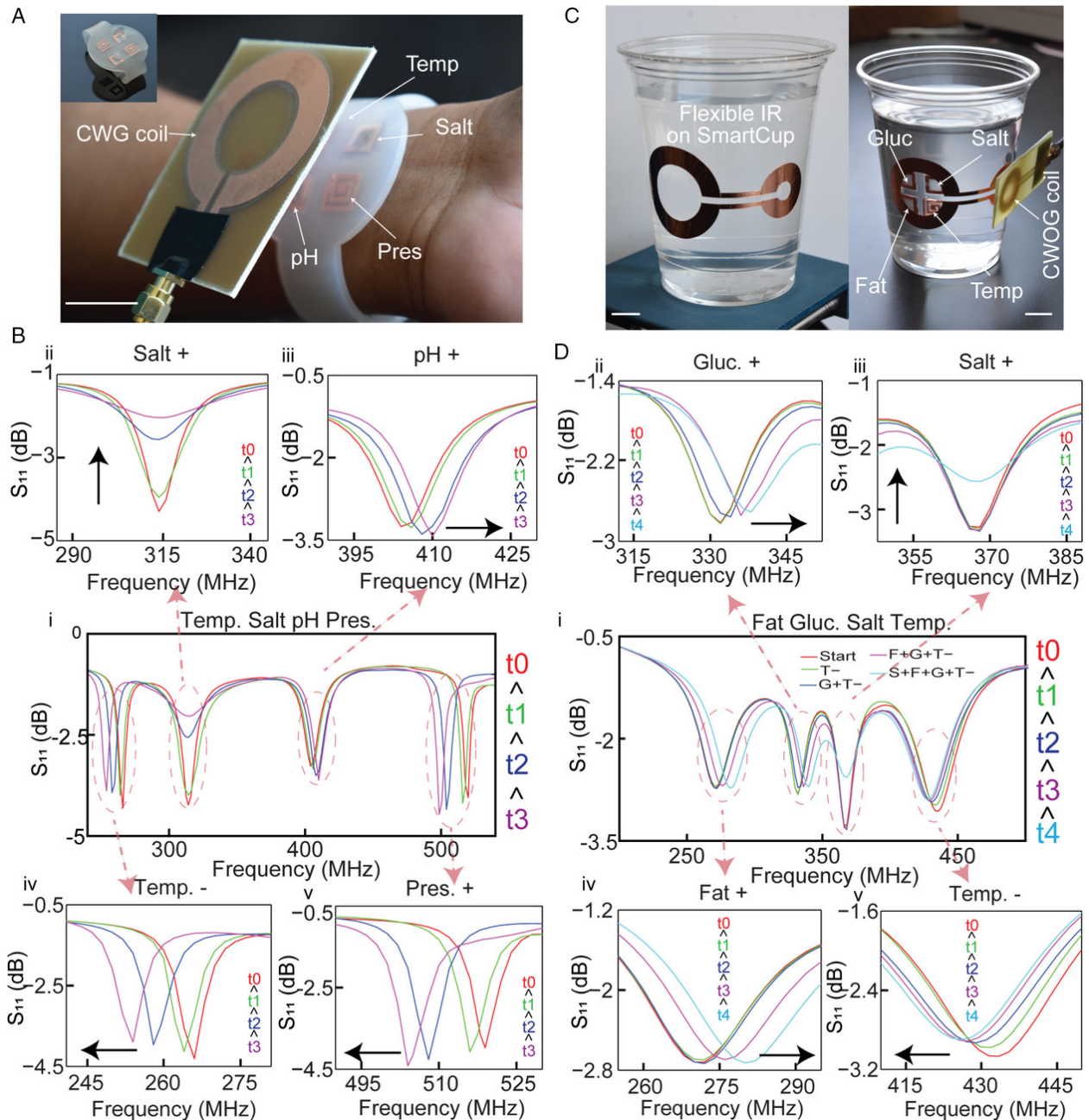
More important is assessing how the perturbation of a single RF sensor may impact the total spectral response of the network (Figure 4.4.3B). Seven pressure sensors were placed on the readout coil and each sensor was perturbed in sequence (Figure S13 for CWOG and S14 for CWG, Supporting Information). In these mechanical sensors, the resonant frequency will shift due to an applied mechanical pressure. For such a static network, for CWOG, CWG, and PWG we found no disturbance/cross-coupling in the total spectra of the network due to the perturbation in individual sensors (Figure 4.4.3Bii,iii, PWG shown

in Figure S15 and S16, Supporting Information). Additionally, no sensimetric coupling is observed with an additional interceding IR element (Figure S17, Supporting Information). In conjunction with measurements on sensor positional coupling, this data suggests that the presence of individual sensors may modulate the induced EM field around the readout coil with ungrounded readout (thus perturbing measurements if sensors are removed), however individual sensor response does not directly cross-couple to the total network. Importantly, this implies that with a static and defined network, given any measurement modality used or with/without the presence of an IR, individual sensor response links exclusively to its designated wavelength. As will be seen, such static networks can readily be engineered by embedding coils and sensors along structures with our flexible fabrication protocols.

We implemented such studied passive wireless networks to monitor the chemophysical state of objects and environments relevant to our daily life. The first was with a wristband with four sensors that enable readout of salt, pH, temperature, and pressure simultaneously (sensor structures are shown in Figure S18, Supporting Information). The sensing characteristics of such sensors are presented in a previous study.[29, 30] In general, capacitive-based sensors shift up to 20% in resonant frequency with varying input, while loss-based sensors will modulate up to 80% in magnitude. In this wristband (Figure 4.4A), temperature and pressure sensors are completely sealed within the silicone; however, salt and pH sensors have a bottom side opening to enable access to the sweat. As demonstrated previously, such passive sensors can individually be read out wirelessly without any microelectronics at the sensing node. Such sensors can be monitored with an intermediate relay fused on the textile (Figure 4.4.1B), or directly with the readout as shown in Figure 4.4A. As CWG elicits a higher magnitude response if there is no IR, we used a 5 cm CWG antenna to read sensor response simultaneously through direct readout. We tested the ability of our sensors to monitor analytical-to-physical signals around human subjects (Figure 4.4B). Typical probing power for VNA (wearable and otherwise) maxes out at around -6 to -5 dBm (300 mW). This is below near-field communication power standards (1 W), which have a measured specific

absorption rate of over an order of magnitude below upper limits for the human body.[45] We estimate that the allowed maximum power would be a bit over an order of magnitude greater than our current VNA (around the power limit utilized in most Qi chargers, 10 W). This type of excess power is unnecessary if sensors are well-designed around bodily stimuli. Figure 4.4Bi shows the originally recorded spectra and modified spectra, where individual ii) salt, iii) pH, iv) temperature, and v) pressure sensor response are shown in a larger view. The stimuli were generated individually as follows (to validate the lack of cross-coupling among sensors): the temperature sensor was heated by the hot air flow, pressure sensor was mechanically stimulated by various weights, NaCl was added to the salt sensors, while deionised (DI) water was added to the pH sensor. As expected, the resonant frequency of the temperature sensor decreases while cooling as the permittivity of the PEG -1500 interlayer material increases at lower temperatures. The resonant frequency of the pressure sensor decreases with pressure as pressure decreases the interlayer thickness. The magnitude of the signal of the salt sensor decreases as salt penetrates and increases the conductivity of the interlayer PEGDA700 hydrogel. The resonant frequency of the pH sensor increases with the DI water (pH = 7), as the p(NIPAM-co-AA) swells from pH 4 to pH 7. Such a wearable wristband enables a passive and wireless multiparametric readout of the bodily state without any electronics required on the body.

To characterize a functional network containing an IR, we developed a Smartcup that is integrated with our recently developed novel biosensors (sensor structures shown in Figure S19, Supporting Information) for the discrimination and readout of nutrients directly from food.[35] In the previous study, we utilized multiscale engineering of silk biopolymer-interlayer constructs to synthesize different sensors tuned to directly measure salts, sugars, and fat content from food. A major advantage of the spectral approach demonstrated herein is that we can measure our varying optimized nutrient sensors simultaneously, easing the readout of multiple nutrients in complex inputs. We additionally utilized a temperature sensor alongside three optimized nutrient sensors (tuned to salt, sugar, and fat) in the in-



ner side of the Smartcup. These sensors were carefully aligned to an IR that was fixed on the outer side of the smart cup. This forms a stable, passive wireless network with zero-electronics that is affixed on a cup. As CWOOG elicits a higher magnitude response from the network if an IR is used, we used a 2.5 cm CWOOG antenna with the IR to read the sensor response simultaneously shown in Figure 4.4C (left: placement of a flexible IR on the Smartcup, right: placement of the sensor, IR, and antenna). We performed testing of the nutrient monitoring from the Smartcup, which reports on temperature, salt, sugar, and fat (Figure 4.4D). Figure 4.4D i) is the original recorded signal and modulated response, where ii) glucose, iii) salt, iv) fat, and v) temperature sensor temporal response is each highlighted in a larger view. These sensors have previously been validated to measure nutrient content while directly exposed to foods (teas, meat, milk, etc.); however, they do exhibit sensimetric cross-coupling in nutrient response because they are partially selective (this is decoupled using postprocessing analysis). Here, to properly validate that individual sensors do not cross-couple to the full spectra of the network each biosensor is probed in a mini-well through individual perturbation of their respective target nutrient. In addition, all sensors exhibit a response time that must be monitored. The temperature sensor was heated to 50°C and let it cool in a 40°C environment, validating the temperature sensor response does not elicit a change in the readout of other sensors. Glucose was then added to the sugar biosensor, and this increased the resonant frequency due to biopolymer swelling. At the same time, the temperature sensor is still modulating to a lower frequency because of residual lag in the temperature sensor response; however, the remaining sensors still do not exhibit any change as they have not undergone perturbation. Next, oleic acid is added to the fat sensor, where the replacement of high-permittivity water with low-permittivity oleic acid reduces the capacitance of the structure. Now all the sensors except the salt-optimized biosensor are exhibiting expected temporal shifts in accordance with the characteristics of the individual sensor. Finally, we added NaCl to the salt sensor, which increases the conductivity of the interlayer silk and reduces the signal Q/magnitude. The complete spectra of the Smartcup

stabilize to their final state in accordance with the final state of each individual temperature or nutrient sensor. This validates the measurement capabilities of flexible/reactive passive networks in a practical setting.

Chapter 5

Passive Wireless Body

Joint-Monitoring Networks with Textile-Integrated, Strongly Coupled Magnetic Resonators

5.1 Operating Principle

As shown in Figure 5.1a, two strongly coupled resonators and a reader antenna are placed across the joint with a separation distance. Flexion is achieved when the forearm rotates with respect to the upper arm about the center of the joint. At full extension, the arms are straight and the flexion angle is 180° . As the forearm flexes about the joint, the flexion angle decreases. Similarly, the forearm may also rotate about the joint. In both flexion and rotation scenarios, the two resonators get misaligned, leading to changes in the coupling coefficient. In turn, such changes can be monitored to identify the exact flexion or rotation

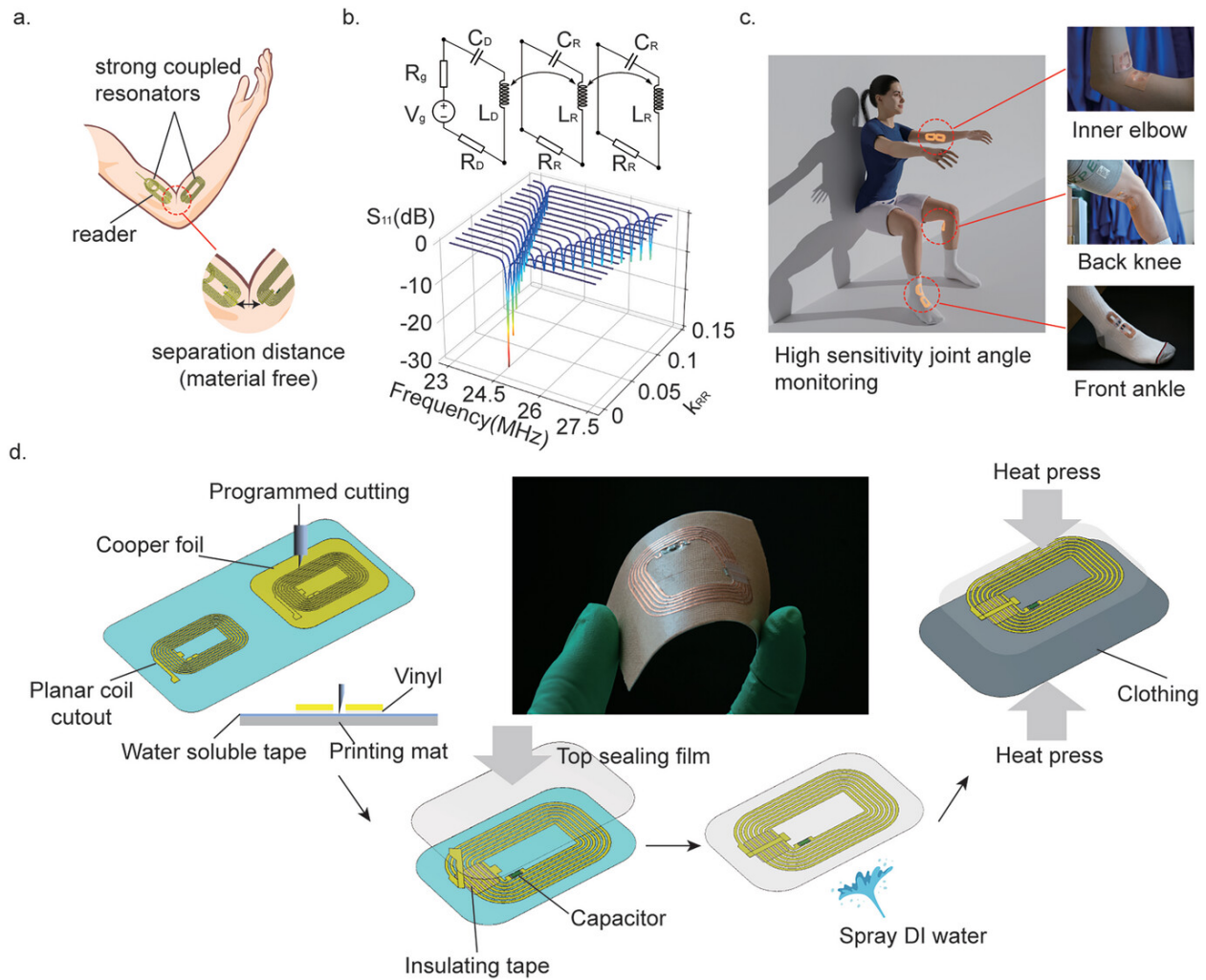


Figure 5.1: Design of strongly coupled resonators for joint angle monitoring. a) Diagram of sensing mechanism. b) Equivalent circuit of the strongly coupled resonators and resonance split with respect to coupling coefficient. c) Multiple joint monitoring diagram. d) Sensor fabrication and integration into textile.

angles.

As shown in Figure 5.1b, each magnetically strongly coupled resonator consists of a multiturn planar loop with a self-inductance of L , an effective ohmic resistance R including self-resistance and fringing electric currents caused by background lossy media. The resonance properties of this building block are determined by the effective capacitance, which consists of the structural stray and a discrete tuning component of capacitance C . We incorporate a lumped surface mount capacitor to dominate the stray capacitance (larger by

an of n order of magnitude) to achieve a stable resonant response that is insensitive to skin proximity. Traditionally, the resonance characteristics of a circuit with a coupled inductor are calculated through Kirchhoff's voltage law and differentiating both equations with respect to time to eliminate the integral term. Let us assume no damping (resistances R are negligible) and focus on the resonant frequencies. For each resonator circuit

$$L_R d^2 I / dt^2 + I / C_R + M_{RR} d^2 I / dt^2 = 0 \quad (5.1)$$

We assume that the current I flowing in resonators has a sinusoidal time dependency with angular frequency ω . Thus, solutions will be of the form $I = Ae^{j\omega t}$. For nontrivial solutions of A, the determinant of the coefficient matrix must be zero

$$\begin{vmatrix} -\omega^2 L_R + 1/C_R & -\omega^2 M \\ -\omega^2 M & -\omega^2 L_R + 1/C_R \end{vmatrix} = 0$$

which leads to the following characteristic equation

$$\omega^4 (L_R^2 - M_{RR}^2) - \omega^2 2L_R / C_R + 1 / C_R^2 = 0 \quad (5.2)$$

Solving this quadratic equation for ω_2 will give us the squared angular frequencies of the system. The frequency split is explicitly related to the mutual inductance MRR. The resistances in the circuits introduce energy dissipation, which affects the amplitude and the phase of the oscillations, as well as the resonant frequencies to a lesser extent. The detailed analysis with resistance included can still be carried out analytically (Figure S1, Supporting Information). The exact numerical solutions are calculated in MATLAB R2020b and

validated in Advanced Design System 2020, Keysight.

Though the joints studied in later exercises will be knee and ankle joints, the resonator is readily applicable to other joints (Figure 5.1c) and easy to fabricate (Figure 5.1d). The coil trace is cut out of copper. After being tuned by a capacitor and soldered flipped trace, the layers are first stacked from the top, then sprayed to get rid of the bottom holder layer, and finally placed on the clothing to be fixed by heat pressing (the Experimental Section). Our resonator footprint is 31 mm by 48.4 mm. This size was chosen because it effectively measures joint movements. When using smaller-sized resonators, the coupling between two resonators will be weaker, thus the resonators may fail to measure very large angles (reducing the operation range of the approach). As resonators increase in size, they may become impractical to fit onto clothing and/or begin to restrict motion. In general, smaller-sized resonators may have improved resolution/sensitivity due to larger shifts in the resonant frequency split, however, their operation range becomes limited. This reflects the fundamental tradeoff encountered in this technique.

5.2 Simulation and Calibration

We first validated our paired strongly coupled resonators as potential joint monitors in a benchtop setting. The employed setup is shown in Figure 5.2a. The right resonator is kept straight, bent horizontally, or bent vertically to mimic potential deformation states when attached to actual human joints. For example, the horizontal bending state would match when the top resonator is placed above the shin, while the vertical bending state would match when the top resonator is placed above the bicep. Simulated magnetic fields at a flexion angle 30° are shown in Figure 5.2b. We notice there is a stronger magnetic field when the deformation effectively brings the two coils closer to each other. This contributes to stronger mutual coupling and consequently widens the resonance frequency split (Figure 5.2c). For example, if

the top resonator is vertically bent, it effectively leads to larger frequency split as compared to other deformation states as the middle of the resonator protrudes closer to its pair (at equivalent bending angles). This has implications for the practical sensitivity of measuring different joints, which may modulate the initial deformation state of the resonators. Due to the shape of different joints, the inductor will possess curvature due to the natural shape of the body. This curvature modulates how this inductor interacts with its pair on the other joints, changing the resonant frequency split as well as how much this frequency split changes with joint flexion. This is because the coupling is impacted by the curvature. As a complete picture, Figure 5.2d plots both the simulated and experimentally measured resonance frequency split from 30° to 110° . Here, a protractor is used to fix the angle between coils, allowing for benchtop validation of resonator performance. For experimental data, we measured three times with an error bar applied (standard deviation). Smaller angles generally exhibit the most deviation in the measurement. We found this to be a result of inaccuracy in our ability to mechanically repeat the same angle. When the resonators are extremely close together, they are highly sensitive to slight deviations in orientation/alignment.

We further performed studies on how resonator placement (with respect to lateral displacement) impacts the spectral response of the paired resonators (Figure S2, Supporting Information). A reduction in lateral separation distance leads to an increased frequency split (measured at 90° bend). This effect is consistent across other bend angles ranging from 30° to 110° , where a decreased lateral distance between resonators enhances the coupling coefficient. In practical on-body experiments, adjustments may be made to the separation distance to account for differences in joint shape and muscle volume, ensuring that movement flexibility remains a priority. We further studied the placement of the reader coil in relation to a single resonator (Figure S3, Supporting Information), to identify an optimal configuration for the strongest coupling. Our primary aim here is to produce a more pronounced S11 valley in the spectrum, effectively improving the repeatability or resolution of our readout. Lastly, we studied how adjustments to the resonators' tuning capacitance (Figure S4, Supporting

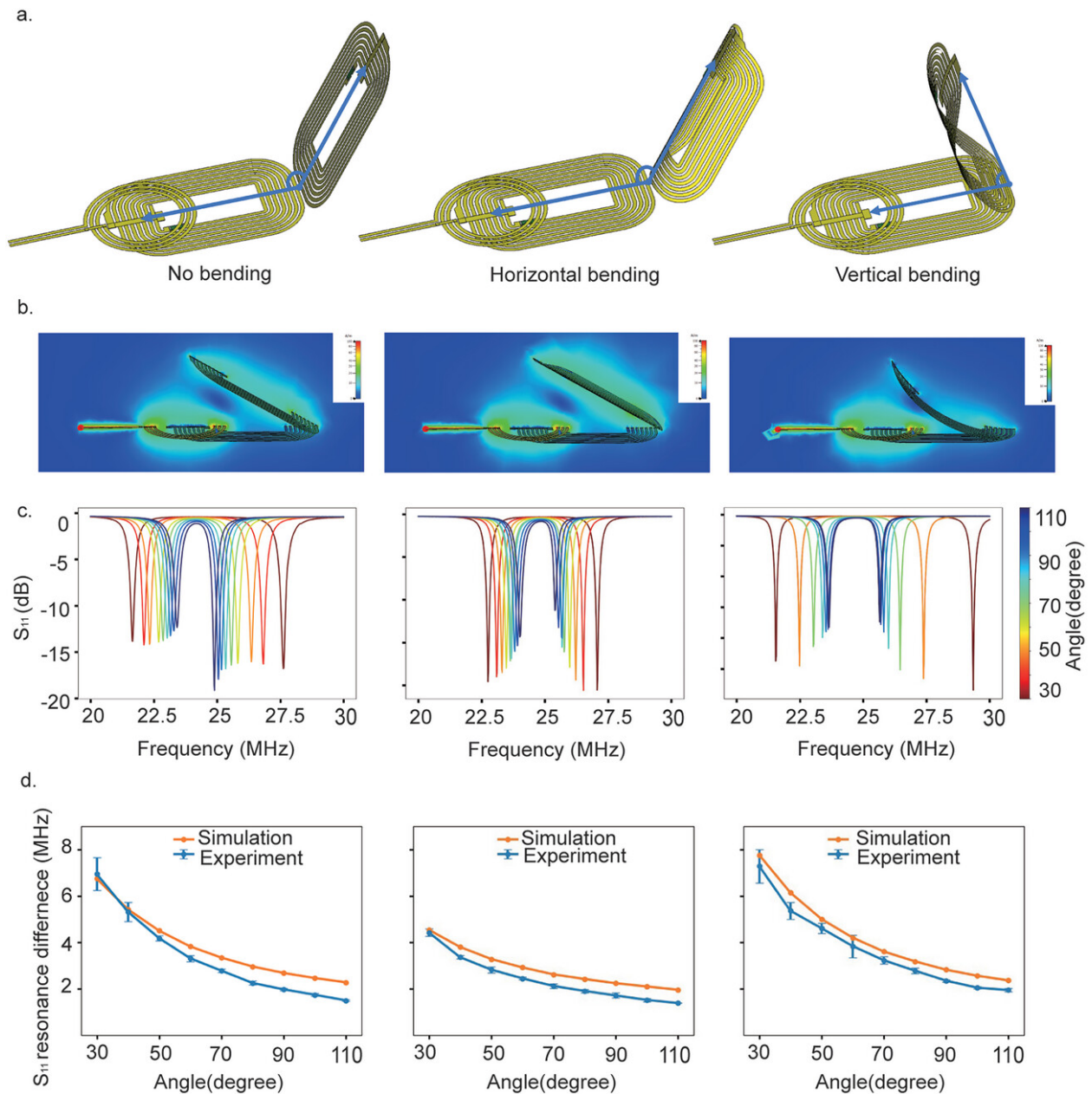


Figure 5.2: Simulation and validation of inductive joint monitoring scheme. a) Resonators can be shaped in simulation to mimic how they may be practically deformed on the curvature of the body. b) Magnetic field distribution at equivalent bending angles for different resonator deformation states. c) Simulated spectral response of resonator pair at different bending angles (30° to 110° every 10°). d) Comparison of the resonant frequency difference between simulation and experiment at different bending angles. $N = 3$ with error bars denoting standard deviation in measured frequency differential.

Information) impact resonator behavior. Increasing capacitance leads to a decrease in both the resonance frequency and the quality factor (Q) of the resonators. Thus, while we may desire a large tuning capacitor to stabilize resonator spectral behavior on the body, using excessively large capacitors may impact readout resolution. Such simulations offer insights into how resonators may be tuned, adjusted, positioned, or optimized for on-body readout.

We next evaluated the response of the resonator pairs to various movements such as supination, extension, and flexion on the human body. Here, the imaging tool MediaPipe is used to calibrate our system, where coil resonant frequency split can be mapped onto angles as determined via imaging. Figure 5.3a–d illustrates the use of resonator pairs to track movements of the elbow, ankle, and knee. As shown in Figure 5.3a, the resonators were first attached to the forearm and upper arm, leaving the elbow free to move, and allowing for the measurement of the reflection coefficient as the elbow rotates. We recorded S11 values for every 45° from 0° to 180°. We also tracked the bending motions of the elbow from 60° to 140° in 10° increments in Figure 5.3b. As can be seen in our measured data, while rotations can be measured via our EM scheme, it is significantly more sensitive to bending as this generates larger resonator distances and thus larger frequency split changes. Exact angle is only able to be estimated knowing the exact motion of the user, this is due to the slight sensitivity of the system to subtle rotations. In a similar manner, we tested our scheme to monitor the bending motions of the ankle (Figure 5.3c) and knee (Figure 5.3d), where we recorded from 100° to 170° and 90° to 170°, respectively. Body joints were fixed at different angles (in this case determined by MediaPipe Body Tracking), and we swept through increasing angles and measured the frequency split at these angles. This experiment is repeated three times, with mean and standard deviation plotted in the figure. All joint images were captured perpendicularly to the camera view to minimize measurement errors. It is important to note that spectral measurements can be highly individualized, as the coils are placed directly on the skin, and factors such as muscle volume can affect the S11 peak-to-peak distance. This leads to variations from person to person and joint to joint.

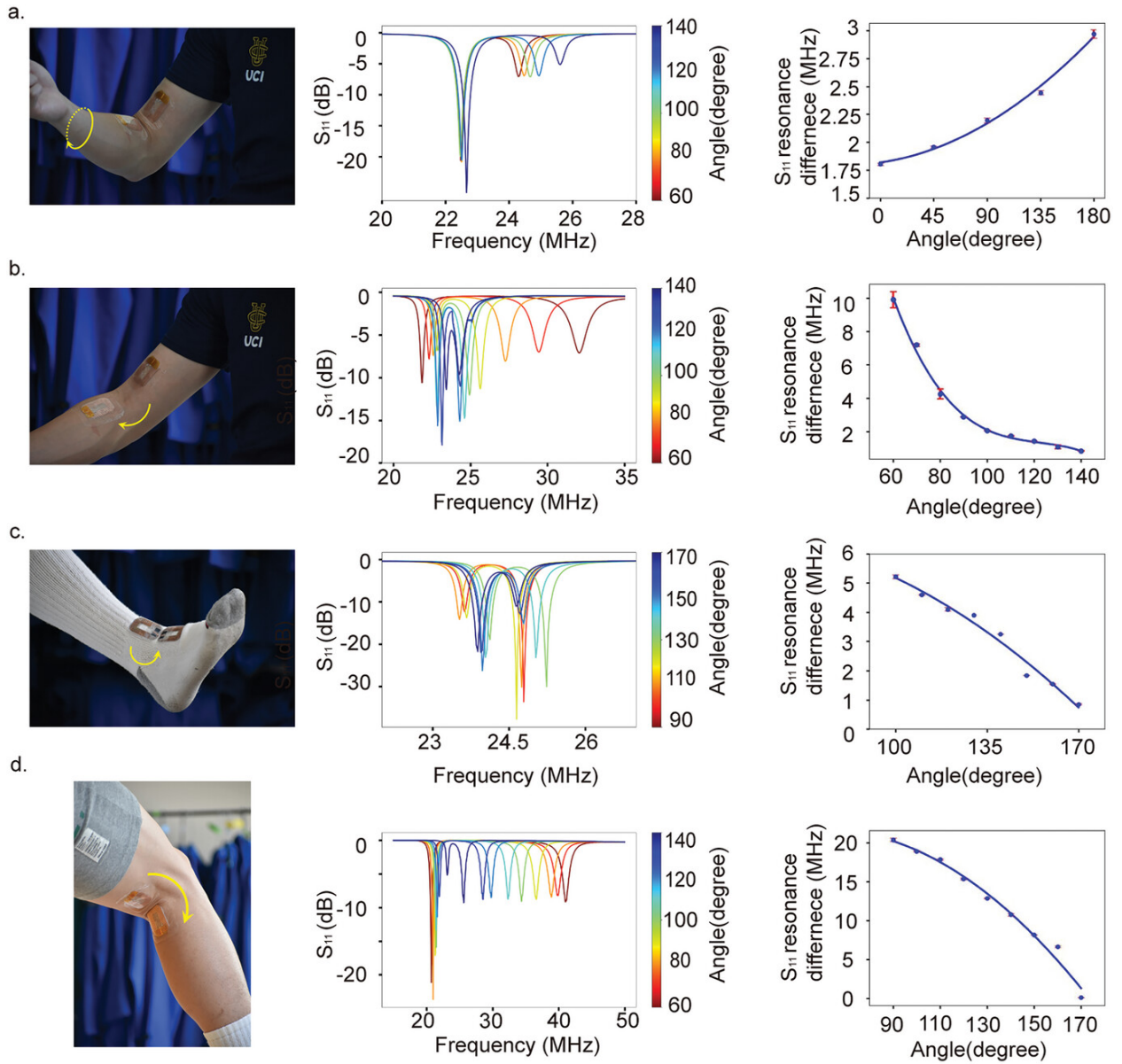


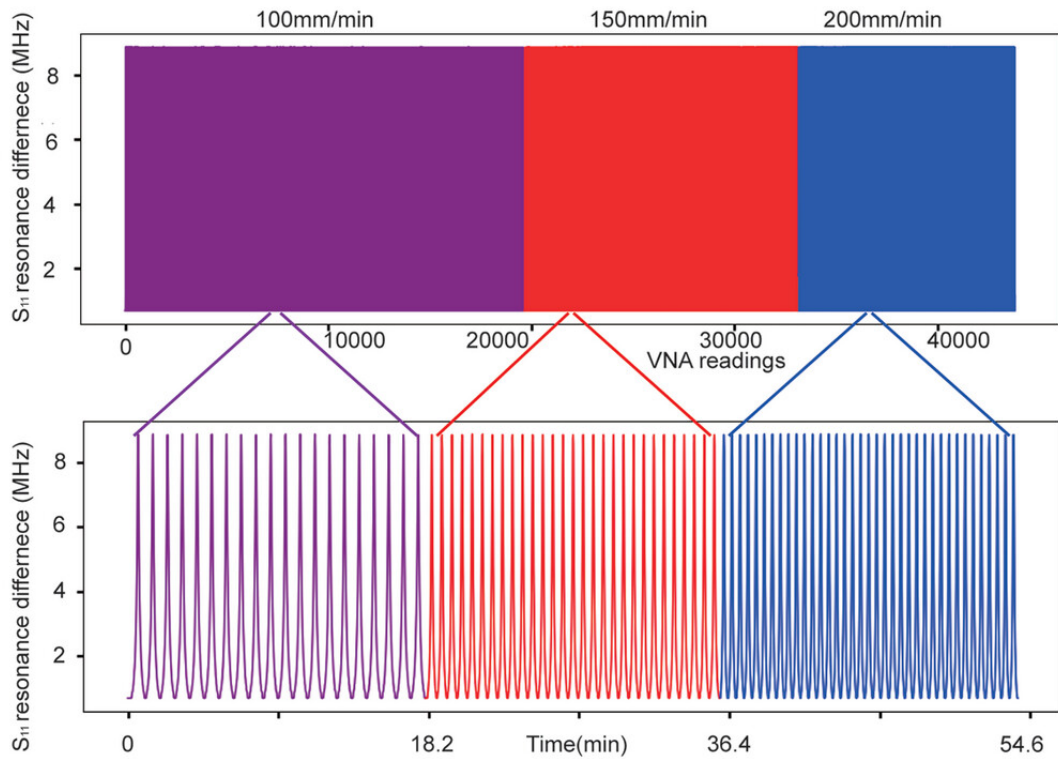
Figure 5.3: On-body joint angle measurement and calibration. The spectral response of our resonator scheme is plotted and compared against image-based body angle tracking. a) Resonators are attached to the elbow for rotation angle monitoring. b) Resonators are attached to elbow for bending/flexing angle monitoring. c) Resonators are attached to ankle for bending/flexing angle monitoring. d) Resonators are attached to the back knee for bending/flexing angle monitoring. The average for $N = 3$ and error bars represent the standard deviation for the right four plots.

5.3 Body Joint Monitoring Networks

To further validate our schemes' benchtop measurement capabilities, we examined the stability of our spectral measurement across three distinct movement speeds, conducting the test 1200 times to verify their durability, as shown in Figure 5.4a. By stacking one coil above the other and oscillating it vertically, we mimicked the dynamic variations in coupling coefficients seen during joint motion. Unlike material strategies such as strain gauges, our studied methodology effectively decouples the sensor output from the position of the largest strain (for the body this is along the joint), and as expected this approach leads to a highly repeatable angular measurement in benchtop settings.

To explore the practical application of our paired strongly coupled resonators for on-body use, we conducted a series of tests to determine the system's ability to distinguish between various physical exercises. For modified clothing, the resonator position was tuned to the individual user. The test subject first puts on the clothing (socks and knee brace), and optimal resonator locations are marked. Subsequently, we embedded the resonator pairs to those marked positions at the ankle and knee, forming joint monitoring networks to monitor key joints along the leg. We expect that generic, nonuser-optimized inductive textiles could be generated (just as all socks, armbands, etc., are standardized), however, their sensitivity could potentially be reduced as inductors are not oriented optimally. The test subject then performed a set of exercises consistently. Figure 5.4b illustrates the initial and final positions for exercises including high knees, push-ups, squats, and lunges. Our detection setup (Figure S5, Supporting Information), consists of a miniVNA and readout coil that is practically affixed to the body adjacent to the inductor coils. The corresponding measured spectral response of initial and final positions for exercises is shown in Figure S6 of the Supporting Information. Notably, the high knee and squat exercises involve significant movement in both the knee and ankle joints, whereas during push-ups and lunges, the knee joint remains relatively stable, and the ankle joint only exhibits slight bending. These exercises thus lead

a.



b.

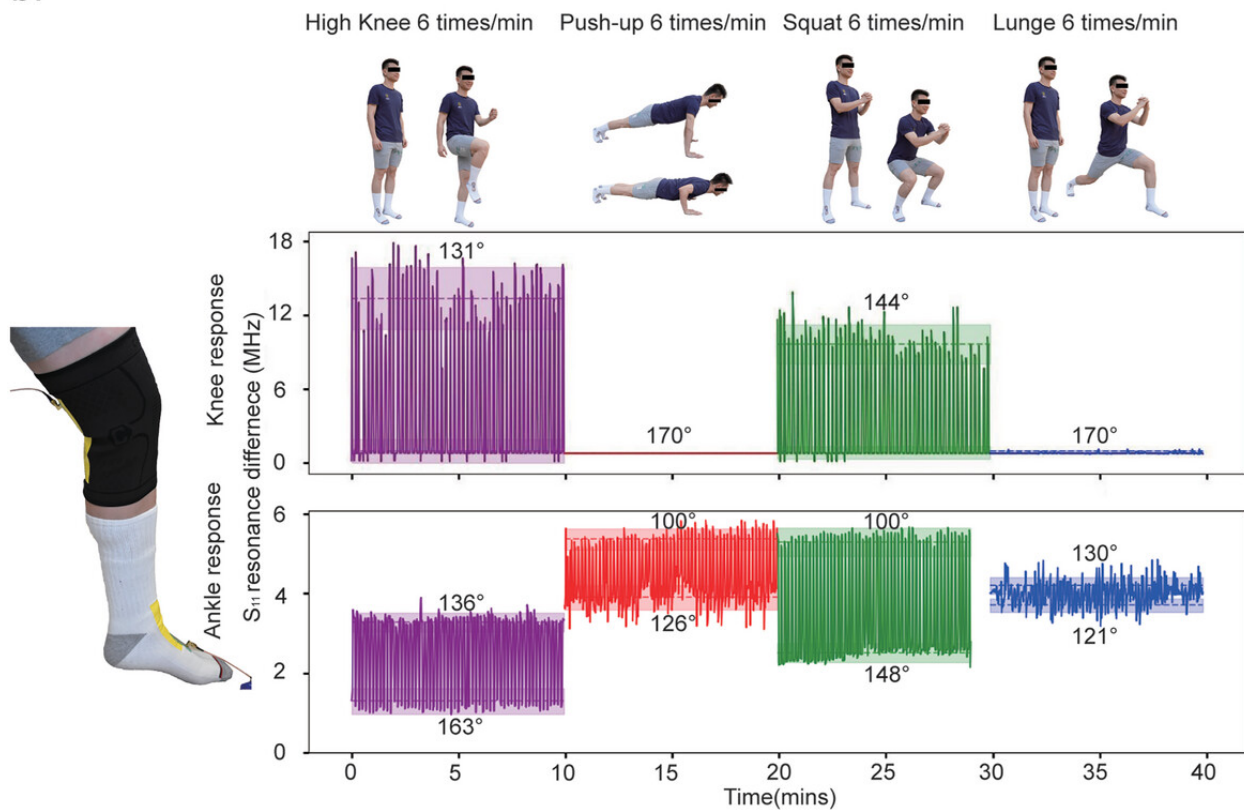


Figure 5.4: Passive joint monitoring networks. a) Dynamic spectral response of resonator pair in benchtop settings. b) Real-time monitoring of knee and ankle joints during a variety of practical exercises. Each exercise exhibits unique signatures in measured joint angle response along the knee and ankle, respectively. With the plots, the mean joint angle (as measured using user pictures) is labeled for respective exercises.

to clear different signatures in the multijoint monitoring scheme, which can potentially be used to recognize different activities. Of course, despite efforts to maintain consistency in the movements, some variability will occur during exercise as natural motion is imperfect. We used the interquartile range to filter out abnormal data and determine the lower and upper boundaries. The centroid values of the S11 resonance difference peaks for the four exercises were calculated. These values were then calibrated to specific angles using a rule-based method, based on the findings in Figure 5.3 and Figure S7 (Supporting Information). This strategy is used to map frequency splits to the different approximate measured joint angles as shown in Figure 5.4b. In this experiment, the optical system calibration is not necessary as it only needs to be carried out once to understand the individualized nature of angle/resonator configuration from person to person. From this point on the imaging is not necessary. It is possible that this imaging step can be removed altogether through more advanced simulation and knowing person-to-person resonator configurations.

As shown in Figure 5.3, there may be some error in our measurement that can potentially be related to the standard deviation encountered during our studies (corresponding to around $\pm 2^\circ$). For faster motion, the accuracy of the VNA measurement will depend on its refresh rate. A higher refresh rate is necessary for capturing extremes in rapid motion, and if the refresh rate is not high enough our approach will have a larger error than encountered for our stretch measurements. Additionally, it's important to note that our calibration tool, MediaPipe, can be prone to errors in measurements. To minimize these errors, all joint images were captured perpendicularly to the camera view.

Bibliography

- [1] S. Amendola, L. Bianchi, and G. Marrocco. Movement detection of human body segments: Passive radio-frequency identification and machine-learning technologies. *IEEE Antennas and Propagation Magazine*, 57(3):23–37, 2015.
- [2] W. Aoi, X. Zou, J. B. Xiao, and Y. Marunaka. Body fluid ph balance in metabolic health and possible benefits of dietary alkaline foods. *Efood*, 1(1):12–23, 2020.
- [3] T. Aoki, B. Dayan, E. Wilcut, W. P. Bowen, A. S. Parkins, T. Kippenberg, K. Vahala, and H. Kimble. Observation of strong coupling between one atom and a monolithic microresonator. *Nature*, 443(7112):671–674, 2006.
- [4] M. Babor, H. M. Greenblatt, M. Edelman, and V. Sobolev. Flexibility of metal binding sites in proteins on a database scale. *Proteins: Structure, Function, and Bioinformatics*, 59(2):221–230, 2005.
- [5] R. Barer, A. Cole, and H. Thompson. Infra-red spectroscopy with the reflecting microscope in physics, chemistry and biology. *nature*, 163(4136):198–201, 1949.
- [6] M. Bargagli, P. M. Ferraro, M. Vittori, G. Lombardi, G. Gambaro, and B. Somani. Calcium and vitamin d supplementation and their association with kidney stone disease: a narrative review. *Nutrients*, 13(12):4363, 2021.
- [7] V. Bonnet, V. Joukov, D. Kulić, P. Fraisse, N. Ramdani, and G. Venture. Monitoring of hip and knee joint angles using a single inertial measurement unit during lower limb rehabilitation. *IEEE Sensors journal*, 16(6):1557–1564, 2015.
- [8] F. Bordi, C. Cametti, and R. Colby. Dielectric spectroscopy and conductivity of polyelectrolyte solutions. *Journal of Physics: Condensed Matter*, 16(49):R1423, 2004.
- [9] S. Borrelli, M. Provenzano, I. Gagliardi, A. Michael, M. E. Liberti, L. De Nicola, G. Conte, C. Garofalo, and M. Andreucci. Sodium intake and chronic kidney disease. *International journal of molecular sciences*, 21(13):4744, 2020.
- [10] A. Botturi, V. Ciappolino, G. Delvecchio, A. Boscutti, B. Viscardi, and P. Brambilla. The role and the effect of magnesium in mental disorders: a systematic review. *Nutrients*, 12(6):1661, 2020.

- [11] C. M. Boutry, L. Beker, Y. Kaizawa, C. Vassos, H. Tran, A. C. Hinckley, R. Pfattner, S. Niu, J. Li, J. Claverie, et al. Biodegradable and flexible arterial-pulse sensor for the wireless monitoring of blood flow. *Nature biomedical engineering*, 3(1):47–57, 2019.
- [12] M. A. Buffington and K. Abreo. Hyponatremia: a review. *Journal of intensive care medicine*, 31(4):223–236, 2016.
- [13] H. J. Butler, P. M. Brennan, J. M. Cameron, D. Finlayson, M. G. Hegarty, M. D. Jenkinson, D. S. Palmer, B. R. Smith, and M. J. Baker. Development of high-throughput atr-ftir technology for rapid triage of brain cancer. *Nature communications*, 10(1):4501, 2019.
- [14] P. Campbell, I. Moore, and M. Pearson. Laser spectroscopy for nuclear structure physics. *Progress in Particle and Nuclear Physics*, 86:127–180, 2016.
- [15] A. R. Carr, Y. H. Patel, C. R. Neff, S. Charkhabi, N. E. Kallmyer, H. F. Angus, and N. F. Reuel. Sweat monitoring beneath garments using passive, wireless resonant sensors interfaced with laser-ablated microfluidics. *NPJ digital medicine*, 3(1):62, 2020.
- [16] M. F. Carroll and D. S. Schade. A practical approach to hypercalcemia. *American family physician*, 67(9):1959–1966, 2003.
- [17] W. H. Chan, R. H. Yang, and K. M. Wang. Development of a mercury ion-selective optical sensor based on fluorescence quenching of 5, 10, 15, 20-tetraphenylporphyrin. *Analytica Chimica Acta*, 444(2):261–269, 2001.
- [18] L. Chen, B. Tee, A. Chortos, G. Schwartz, and V. Tse. J. lipomi, d.; wong, h.-sp; mcconnell, mv; bao, z. continuous wireless pressure monitoring and mapping with ultra-small passive sensors for health monitoring and critical care. *Nat. Commun*, 5:1–10, 2014.
- [19] M. Choi, G. Douberly, T. Falconer, W. Lewis, C. M. Lindsay, J. Merritt, P. Stiles, and R. Miller. Infrared spectroscopy of helium nanodroplets: novel methods for physics and chemistry. *International Reviews in Physical Chemistry*, 25(1-2):15–75, 2006.
- [20] G. Corso, C. Colavita, M. Esposito, R. Roma, C. Napoli, M. Zamparelli, and V. Ansanelli. Gaschromatography-mass spectrometry analysis of fatty acids in human milk from forty puerperae living in southern italy. *Rivista Europea per le Scienze Mediche e Farmacologiche= European Review for Medical and Pharmacological Sciences= Revue Europeenne Pour les Sciences Medicales et Pharmacologiques*, 17(6):215–219, 1995.
- [21] J. T. Costello, J.-P. Mosnier, E. T. Kennedy, P. Carroll, and G. O’Sullivan. X-uv absorption spectroscopy with laser-produced plasmas: a review. *Physica Scripta*, 1991(T34):77, 1991.
- [22] P. Damala, E. Zdrachek, T. Forrest, and E. Bakker. Unconditioned symmetric solid-contact electrodes for potentiometric sensing. *Analytical Chemistry*, 94(33):11549–11556, 2022.

- [23] M. Dautta, M. Alshetaiwi, A. Escobar, F. Torres, N. Bernardo, and P. Tseng. Multi-functional hydrogel-interlayer rf/nfc resonators as a versatile platform for passive and wireless biosensing. *Advanced electronic materials*, 6(4):1901311, 2020.
- [24] M. Dautta, M. Alshetaiwi, J. Escobar, and P. Tseng. Passive and wireless, implantable glucose sensing with phenylboronic acid hydrogel-interlayer rf resonators. *Biosensors and Bioelectronics*, 151:112004, 2020.
- [25] M. Dautta, K. K. H. Dia, A. Hajiaghajani, A. R. Escobar, M. Alshetaiwi, and P. Tseng. Multiscale, nano-to mesostructural engineering of silk biopolymer-interlayer biosensors for continuous comonitoring of nutrients in food. *Advanced Materials Technologies*, 7(2):2100666, 2022.
- [26] M. Dautta, A. Hajiaghajani, F. Ye, A. R. Escobar, A. Jimenez, K. K. H. Dia, and P. Tseng. Programmable multiwavelength radio frequency spectrometry of chemophysical environments through an adaptable network of flexible and environmentally responsive, passive wireless elements. *Small Science*, 2(6):2200013, 2022.
- [27] K. K. H. Dia, A. R. Escobar, H. Qin, F. Ye, A. Jimenez, M. A. Hasan, A. Hajiaghajani, M. Dautta, L. Li, and P. Tseng. Passive wireless porous biopolymer sensors for at-home monitoring of oil and fatty acid nutrition. *ACS Applied Bio Materials*, 7(8):5452–5460, 2024.
- [28] X. Du and X. Xie. Ion-selective optodes: Alternative approaches for simplified fabrication and signaling. *Sensors and Actuators B: Chemical*, 335:129368, 2021.
- [29] X. Du, L. Yu, S. Ling, J. Xie, and W. Chen. High-salt diet impairs the neurons plasticity and the neurotransmitters-related biological processes. *Nutrients*, 13(11):4123, 2021.
- [30] X. Du, J. Zhai, X. Li, Y. Zhang, N. Li, and X. Xie. Hydrogel-based optical ion sensors: Principles and challenges for point-of-care testing and environmental monitoring. *ACS sensors*, 6(6):1990–2001, 2021.
- [31] P. Eichelberger, M. Ferraro, U. Minder, T. Denton, A. Blasimann, F. Krause, and H. Baur. Analysis of accuracy in optical motion capture—a protocol for laboratory setup evaluation. *Journal of biomechanics*, 49(10):2085–2088, 2016.
- [32] F. Ferryanto and M. Nakashima. Development of a markerless optical motion capture system for daily use of training in swimming. *Sports Engineering*, 20:63–72, 2017.
- [33] M. Fibbioli, W. E. Morf, M. Badertscher, N. F. de Rooij, and E. Pretsch. Potential drifts of solid-contacted ion-selective electrodes due to zero-current ion fluxes through the sensor membrane. *Electroanalysis: An International Journal Devoted to Fundamental and Practical Aspects of Electroanalysis*, 12(16):1286–1292, 2000.
- [34] E. Gałęska, M. Wrzecińska, A. Kowalczyk, and J. P. Araujo. Reproductive consequences of electrolyte disturbances in domestic animals. *Biology*, 11(7):1006, 2022.

- [35] A. Hajiaghajani, A. H. Afandizadeh Zargari, M. Dautta, A. Jimenez, F. Kurdahi, and P. Tseng. Textile-integrated metamaterials for near-field multibody area networks. *Nature Electronics*, 4(11):808–817, 2021.
- [36] A. Hajiaghajani, P. Rwei, A. H. Afandizadeh Zargari, A. R. Escobar, F. Kurdahi, M. Khine, and P. Tseng. Amphibious epidermal area networks for uninterrupted wireless data and power transfer. *Nature Communications*, 14(1):7522, 2023.
- [37] A. Hajiaghajani and P. Tseng. Microelectronics-free, augmented telemetry from body-worn passive wireless sensors. *Advanced Materials Technologies*, 6(4):2001127, 2021.
- [38] R. P. Heaney. Role of dietary sodium in osteoporosis. *Journal of the American College of Nutrition*, 25(sup3):271S–276S, 2006.
- [39] L. Herda, P. Fua, R. Plänklers, R. Boulic, and D. Thalmann. Using skeleton-based tracking to increase the reliability of optical motion capture. *Human movement science*, 20(3):313–341, 2001.
- [40] F. Horak, L. King, and M. Mancini. Role of body-worn movement monitor technology for balance and gait rehabilitation. *Physical therapy*, 95(3):461–470, 2015.
- [41] S. Huang, Z. Li, and K. Lu. Transfer efficiency analysis of wireless power transfer system under frequency drift. *Journal of Applied Physics*, 117(17), 2015.
- [42] E. Innes, H. H. Yiu, P. McLean, W. Brown, and M. Boyles. Simulated biological fluids—a systematic review of their biological relevance and use in relation to inhalation toxicology of particles and fibres. *Critical Reviews in Toxicology*, 51(3):217–248, 2021.
- [43] M. T. Islam, M. Samsuzzaman, S. Kibria, N. Misran, and M. T. Islam. Metasurface loaded high gain antenna based microwave imaging using iteratively corrected delay multiply and sum algorithm. *Scientific reports*, 9(1):17317, 2019.
- [44] S.-M. Jeong, M. Son, Y. Kang, J. Yang, T. Lim, and S. Ju. Development of multi-angle fiber array for accurate measurement of flexion and rotation in human joints. *npj Flexible Electronics*, 5(1):35, 2021.
- [45] K. Jomova, M. Makova, S. Y. Alomar, S. H. Alwasel, E. Nepovimova, K. Kuca, C. J. Rhodes, and M. Valko. Essential metals in health and disease. *Chemico-biological interactions*, 367:110173, 2022.
- [46] D. A. Kalashnikov, A. V. Paterova, S. P. Kulik, and L. A. Krivitsky. Infrared spectroscopy with visible light. *Nature Photonics*, 10(2):98–101, 2016.
- [47] N. Kim, R. Dhakal, K. Adhikari, E. Kim, and C. Wang. A reusable robust radio frequency biosensor using microwave resonator by integrated passive device technology for quantitative detection of glucose level. *Biosensors and Bioelectronics*, 67:687–693, 2015.

- [48] A. Krasnok, M. Caldarola, N. Bonod, and A. Alú. Spectroscopy and biosensing with optically resonant dielectric nanostructures. *Advanced optical materials*, 6(5):1701094, 2018.
- [49] I. Y. Kuo and B. E. Ehrlich. Signaling in muscle contraction. *Cold Spring Harbor perspectives in biology*, 7(2):a006023, 2015.
- [50] M. Kussmann, M. Affolter, K. Nagy, B. Holst, and L. B. Fay. Mass spectrometry in nutrition: understanding dietary health effects at the molecular level. *Mass spectrometry reviews*, 26(6):727–750, 2007.
- [51] H.-J. Lee and J.-G. Yook. Recent research trends of radio-frequency biosensors for biomolecular detection. *Biosensors and Bioelectronics*, 61:448–459, 2014.
- [52] L. Li, A. R. Escobar, S. Zanganeh, M. Dautta, M. Sajeeb, F. Ye, J. T. Escobar, and P. Tseng. Mechanically-directed assembly of nanostructured biopolymer with tunable anisotropy, hierarchy, and functionality. *Next Materials*, 2:100140, 2024.
- [53] L. Li, Y.-n. Zhang, Y. Zhou, W. Zheng, Y. Sun, G. Ma, and Y. Zhao. Optical fiber optofluidic bio-chemical sensors: a review. *Laser & photonics reviews*, 15(7):2000526, 2021.
- [54] P. Li and J. Hur. Utilization of uv-vis spectroscopy and related data analyses for dissolved organic matter (dom) studies: A review. *Critical Reviews in Environmental Science and Technology*, 47(3):131–154, 2017.
- [55] L. Lin, M. Dautta, A. Hajiaghajani, A. R. Escobar, P. Tseng, and M. Khine. Paint-on epidermal electronics for on-demand sensors and circuits. *Advanced Electronic Materials*, 7(1):2000765, 2021.
- [56] R. Lin, H.-J. Kim, S. Achavananthadith, S. A. Kurt, S. C. Tan, H. Yao, B. C. Tee, J. K. Lee, and J. S. Ho. Wireless battery-free body sensor networks using near-field-enabled clothing. *Nature communications*, 11(1):444, 2020.
- [57] R. Lin, H.-J. Kim, S. Achavananthadith, Z. Xiong, J. K. Lee, Y. L. Kong, and J. S. Ho. Digitally-embroidered liquid metal electronic textiles for wearable wireless systems. *Nature communications*, 13(1):2190, 2022.
- [58] J. Liu, L. Wang, J. Fang, L. Guo, B. Lu, and L. Shu. Multi-target intense human motion analysis and detection using channel state information. *Sensors*, 18(10):3379, 2018.
- [59] D. M. Lovinger. Communication networks in the brain: neurons, receptors, neurotransmitters, and alcohol. *Alcohol Research & Health*, 31(3):196, 2008.
- [60] D. Lu, Y. Yan, R. Avila, I. Kandela, I. Stepien, M.-H. Seo, W. Bai, Q. Yang, C. Li, C. R. Haney, et al. Bioresorbable, wireless, passive sensors as temporary implants for monitoring regional body temperature. *Advanced Healthcare Materials*, 9(16):2000942, 2020.

- [61] T. P. Luu, S. Nakagome, Y. He, and J. L. Contreras-Vidal. Real-time eeg-based brain-computer interface to a virtual avatar enhances cortical involvement in human treadmill walking. *Scientific reports*, 7(1):8895, 2017.
- [62] Y. Lyu, S. Gan, Y. Bao, L. Zhong, J. Xu, W. Wang, Z. Liu, Y. Ma, G. Yang, and L. Niu. Solid-contact ion-selective electrodes: Response mechanisms, transducer materials and wearable sensors. *Membranes*, 10(6):128, 2020.
- [63] S. Majumder and M. J. Deen. Wearable imu-based system for real-time monitoring of lower-limb joints. *IEEE sensors journal*, 21(6):8267–8275, 2020.
- [64] S. Malangone and C. J. Campen. Hypercalcemia of malignancy. *Journal of the advanced practitioner in oncology*, 6(6):586, 2015.
- [65] N. Mani, P. Haridoss, and B. George. A wearable ultrasonic-based ankle angle and toe clearance sensing system for gait analysis. *IEEE Sensors Journal*, 21(6):8593–8603, 2020.
- [66] J. McNamara and L. Worthley. Acid-base balance: part ii. pathophysiology. *Critical care and resuscitation*, 3(3):188–201, 2001.
- [67] L. Mester, A. A. Govyadinov, S. Chen, M. Goikoetxea, and R. Hillenbrand. Subsurface chemical nanoidentification by nano-ftir spectroscopy. *Nature communications*, 11(1):3359, 2020.
- [68] V. Mishra and A. Kiourti. Wearable electrically small loop antennas for monitoring joint flexion and rotation. *IEEE Transactions on Antennas and Propagation*, 68(1):134–141, 2019.
- [69] W. Moerner. A dozen years of single-molecule spectroscopy in physics, chemistry, and biophysics, 2002.
- [70] M. Mushtaq and T. Pasha. Electrolytes, dietary electrolyte balance and salts in broilers: an updated review on acid-base balance, blood and carcass characteristics. *World’s Poultry Science Journal*, 69(4):833–852, 2013.
- [71] S. Niu, N. Matsuhisa, L. Beker, J. Li, S. Wang, J. Wang, Y. Jiang, X. Yan, Y. Yun, W. Burnett, et al. A wireless body area sensor network based on stretchable passive tags. *nat electron* 2 (8): 361–368, 2019.
- [72] K. O’Brien, G. Scheible, and H. Gueldner. Analysis of wireless power supplies for industrial automation systems. In *IECON’03. 29th Annual Conference of the IEEE Industrial Electronics Society (IEEE Cat. No. 03CH37468)*, volume 1, pages 367–372. IEEE, 2003.
- [73] Q. Pan, D. Gong, and Y. Tang. Recent progress and perspective on electrolytes for sodium/potassium-based devices. *Energy Storage Materials*, 31:328–343, 2020.

- [74] S. Pang, P. Song, X. Sun, W. Qi, C. Yang, G. Song, Y. Wang, and J. Zhang. Dietary fructose and risk of metabolic syndrome in chinese residents aged 45 and above: results from the china national nutrition and health survey. *Nutrition Journal*, 20:1–11, 2021.
- [75] S. Prabhu. *Textbook of General Pathology for Dental Students*. Springer, 2023.
- [76] F. Qi, F. Liang, M. Liu, H. Lv, P. Wang, H. Xue, and J. Wang. Position-information-indexed classifier for improved through-wall detection and classification of human activities using uwb bio-radar. *IEEE antennas and wireless propagation letters*, 18(3):437–441, 2019.
- [77] H. Qin, A. Hajiaghajani, A. R. Escobar, A. H. A. Zargari, A. Jimenez, F. Kurdahi, and P. Tseng. Laser-induced graphene-based smart textiles for wireless cross-body metrics. *ACS Applied Nano Materials*, 6(20):19158–19167, 2023.
- [78] J. S. Rodman and R. J. Mahler. Kidney stones as a manifestation of hypercalcemic disorders: hyperparathyroidism and sarcoidosis. *Urologic Clinics of North America*, 27(2):275–285, 2000.
- [79] R. Room, T. Babor, and J. Rehm. Alcohol and public health. *The lancet*, 365(9458):519–530, 2005.
- [80] H. Saltzman, R. Rajaram, Y. Zhang, M. A. Islam, and A. Kiourti. Wearable loops for dynamic monitoring of joint flexion: A machine learning approach. *Electronics*, 13(12):2245, 2024.
- [81] E. Scarpa, V. Mastronardi, F. Guido, L. Algieri, A. Quattieri, R. Fiammengo, F. Rizzi, and M. De Vittorio. Wearable piezoelectric mass sensor based on ph sensitive hydrogels for sweat ph monitoring. *Scientific reports*, 10(1):10854, 2020.
- [82] P. Sebo, B. Cerutti, and D. M. Haller. Effect of magnesium therapy on nocturnal leg cramps: a systematic review of randomized controlled trials with meta-analysis using simulations. *Family practice*, 31(1):7–19, 2014.
- [83] J. Shin, Z. Liu, W. Bai, Y. Liu, Y. Yan, Y. Xue, I. Kandela, M. Pezhouh, M. R. MacEwan, Y. Huang, et al. Bioresorbable optical sensor systems for monitoring of intracranial pressure and temperature. *Science advances*, 5(7):eaaw1899, 2019.
- [84] N. Srisasiwimon, S. Chuangchote, N. Laosiripojana, and T. Sagawa. Tio₂/lignin-based carbon composited photocatalysts for enhanced photocatalytic conversion of lignin to high value chemicals. *ACS Sustainable Chemistry & Engineering*, 6(11):13968–13976, 2018.
- [85] B. J. Stetter, S. Ringhof, F. C. Krafft, S. Sell, and T. Stein. Estimation of knee joint forces in sport movements using wearable sensors and machine learning. *Sensors*, 19(17):3690, 2019.
- [86] C. J. Stevens. Magnetoinductive waves and wireless power transfer. *IEEE Transactions on Power Electronics*, 30(11):6182–6190, 2014.

- [87] E. E. Stone and M. Skubic. Unobtrusive, continuous, in-home gait measurement using the microsoft kinect. *IEEE Transactions on Biomedical Engineering*, 60(10):2925–2932, 2013.
- [88] J.-Y. Sun, X. Zhao, W. R. Illeperuma, O. Chaudhuri, K. H. Oh, D. J. Mooney, J. J. Vlassak, and Z. Suo. Highly stretchable and tough hydrogels. *Nature*, 489(7414):133–136, 2012.
- [89] A. Szent-Györgyi. Calcium regulation of muscle contraction. *Biophysical journal*, 15(7):707–723, 1975.
- [90] K. Tangvoraphonkchai and A. Davenport. Magnesium and cardiovascular disease. *Advances in chronic kidney disease*, 25(3):251–260, 2018.
- [91] X. Tian, P. M. Lee, Y. J. Tan, T. L. Wu, H. Yao, M. Zhang, Z. Li, K. A. Ng, B. C. Tee, and J. S. Ho. Wireless body sensor networks based on metamaterial textiles. *Nature Electronics*, 2(6):243–251, 2019.
- [92] X. Tian, Q. Zeng, D. T. Nguyen, and J. S. Ho. Textile-integrated phased surfaces for wireless networking of bioelectronic devices. *IEEE Transactions on Antennas and Propagation*, 2023.
- [93] S. Tierney and H. Falch. Bm; hjelme, dr; stokke, bt determination of glucose levels using a functionalized hydrogel-optical fiber biosensor: Toward continuous monitoring of blood glucose in vivo. *Anal. Chem*, 81(9):3630–3636, 2009.
- [94] P. Tseng, B. Napier, L. Garbarini, D. L. Kaplan, and F. G. Omenetto. Functional, rf-trilayer sensors for tooth-mounted, wireless monitoring of the oral cavity and food consumption. *Advanced Materials*, 30(18):1703257, 2018.
- [95] M. D. Walker and E. Shane. Hypercalcemia: a review. *Jama*, 328(16):1624–1636, 2022.
- [96] Q. Wang, Y. Liu, M. Zhang, X. Bai, and Z. Gao. A simple dielectric resonator-based sensor for temperature measurement. *Results in Physics*, 27:104481, 2021.
- [97] Q. Wang, P. Markopoulos, B. Yu, W. Chen, and A. Timmermans. Interactive wearable systems for upper body rehabilitation: a systematic review. *Journal of neuroengineering and rehabilitation*, 14:1–21, 2017.
- [98] Q. Wang and W.-M. Zhao. A comprehensive review of lossy mode resonance-based fiber optic sensors. *Optics and Lasers in Engineering*, 100:47–60, 2018.
- [99] B. D. Wiltshire, M. A. Rafi, and M. H. Zarifi. Microwave resonator array with liquid metal selection for narrow band material sensing. *Scientific Reports*, 11(1):8598, 2021.
- [100] Y. Xiao, Z. Zhang, A. Beck, J. Yuan, and D. Thalmann. Human–robot interaction by understanding upper body gestures. *Presence*, 23(2):133–154, 2014.

- [101] X. Yin, G. Wu, J. Wei, Y. Shen, H. Qi, and B. Yin. Deep learning on traffic prediction: Methods, analysis, and future directions. *IEEE Transactions on Intelligent Transportation Systems*, 23(6):4927–4943, 2021.
- [102] F. Zhang, S. A. Hackworth, W. Fu, C. Li, Z. Mao, and M. Sun. Relay effect of wireless power transfer using strongly coupled magnetic resonances. *IEEE Transactions on Magnetics*, 47(5):1478–1481, 2011.
- [103] H. Zhang, W. Han, K. Xu, Y. Zhang, Y. Lu, Z. Nie, Y. Du, J. Zhu, and W. Huang. Metallic sandwiched-aerogel hybrids enabling flexible and stretchable intelligent sensor. *Nano Letters*, 20(5):3449–3458, 2020.
- [104] X. Zhang, Y. Song, F. Meng, G. Sun, and L. Zhu. Optical fiber based soft curvature sensor with polyvinyl chloride reinforced silicone rubber substrate. *Optik*, 178:567–574, 2019.
- [105] Y. Zhang, J. B. Caccese, and A. Kiourti. Wearable loop sensor for bilateral knee flexion monitoring. *Sensors*, 24(5):1549, 2024.
- [106] Q. Zou, Z. Lei, T. Xue, S. Li, Z. Ma, and Q. Su. Highly sensitive flexible pressure sensor based on ionic dielectric layer with hierarchical ridge microstructure. *Sensors and Actuators A: Physical*, 313:112218, 2020.